LUMINESCENT SOLAR CONCENTRATION OF TYPE-II NANOPLATELETS

A THESIS SUBMITTED TO
THE GRADUATE SCHOOL OF ENGINEERING AND SCIENCE
OF BILKENT UNIVERSITY
IN PARTIAL FULFILLMENT OF THE REQUIREMENTS FOR
THE DEGREE OF
MASTER OF SCIENCE
IN
MATERIALS SCIENCE AND NANOTECHNOLOGY

By
Ilayda Ozkan

August 2024

LUMINESCENT SOLAR CONCENTRATION OF TYPE-II NANOPLATELETS

By Ilayda Ozkan

August 2024

We certify that we have read this thesis and that in our opinion it is fully adequate, in scope and in quality, as a thesis for degree of Master of Science.

Hilmi Volkan Demir (Advisor)

Emine Yegân Erdem

Yusuf Keleştemur

Approved for the Graduation School of Engineering and Science:

Orhan Arıkan

Director of the Graduate School

ABSTRACT

LUMINESCENT SOLAR CONCENTRATION OF TYPE-II NANOPLATELETS

İlayda Özkan

M.Sc. in Materials Science and Nanotechnology

Advisor: Hilmi Volkan Demir

August 2024

The growing demand for renewable energy sources, driven by economic and environmental considerations, has spurred the development of more efficient methods for harnessing solar power. Luminescent solar concentrators (LSCs) are emerging as a promising technology platform owing to their capability to collect and concentrate sunlight delivered to the mounted photovoltaic cells where electrical power is generated. Nanoplatelets (NPLs) draw significant attention as luminophores for LSCs because of our ability to easily alter their optoelectronic properties via tailoring their size, shape, and composition, while making use of advanced architectures of their heterostructures. In this thesis, controlling their composition carefully, CdSe/CdSe$_{1-x}$Te$_x$/CdSe/CdS NPLs in the core/multicrown architecture with type-II band alignment benefitting from their type-II heterostructure's lower emission energies in the solar spectrum and the suppression of their reabsorption losses were synthesized as the LSC luminophores. The physical characteristics and morphology of these hetero-NPLs were systematically investigated with structural analyses. The resulting CdSe/CdSe$_{1-x}$Te$_x$/CdSe/CdS core/multicrown NPLs having high quantum yields (> 90%), broad Stokes shifts, and stability proved to be excellent candidates for high-performance LSCs. Here, we demonstrated LSC devices fabricated using these type-II NPLs with varied compositions of CdSe/CdSe$_{1-x}$Te$_x$/CdSe/CdS ($0.3 \leq x \leq 0.6$). The best-performing fabricated LSC exhibits an optical power conversion efficiency of 7.29%, the highest reported thus far for NPLs. Thanks to their scalability and affordability, these type-II NPLs hold great promise in several applications of LSCs, including those for agriculture in greenhouses, construction of the facades of buildings, and aerospace together with solar panels on satellites and spacecrafts.

Keywords: Colloidal semiconductor nanocrystals, nanoplatelets, type-II band alignment, luminescent solar concentrator, building integrated photovoltaics.

ÖZET

TİP-II NANOLEVHALARININ IŞIYAN GÜNEŞ YOĞUNLAŞTIRICILARI

İlayda Özkan

Malzeme Bilimi ve Nanoteknoloji, Yüksek Lisans

Tez Danışmanı: Hilmi Volkan Demir

Ağustos 2024

Ekonomik ve çevresel faktörler göz önünde bulundurulduğunda yenilenebilir enerji kaynaklarına yönelik artan talep, güneş enerjisinden daha verimli yararlanmak için yeni yöntemlerin geliştirilmesini teşvik etmiştir. Işıyan güneş yoğunlaştırıcılar (IGY), güneş ışığını toplama ve yoğunlaştırma kabiliyetleri sayesinde monte edildikleri fotovoltaik hücreler aracılığıyla elektrik gücü üretir ve bu nedenle yenilenebilir enerji kaynakları alanında umut vadeden bir teknoloji platformu olarak ortaya çıkmaktadır. Nanolevhaların gelişmiş yapılarından faydalanarak boyut, şekil ve kompozisyon kontrolü ile optoelektronik özelliklerini kolayca değiştirebilmemizden dolayı IGY'ler için ışıyıcı olarak dikkat çekmektedir. Bu tez kapsamında, kompozisyonları dikkatlice kontrol edilen çekirdek/çok taçlı mimarideki CdSe/$CdSe_{1-x}Te_x$/CdSe/CdS tip-II hetero-yapısına sahip nanolevhalar güneş tayfındaki düşük emisyon enerjilerinden ve geri soğrulma kayıplarının bastırılmasından yararlanmak için IGY ışıyıcısı olarak sentezlenmiştir. Farklı türden nanolevhaların fiziksel özellikleri ve morfolojisi yapısal analizlerle sistematik bir şekilde incelenmiştir. Yüksek kuantum verimine (> %90), uzun Stokes kaymasına ve kararlılığa sahip CdSe/$CdSe_{1-x}Te_x$/CdSe/CdS çekirdek/çok taçlı nanolevhaların yüksek performanslı IGY'ler için mükemmel adaylar olduğu kanıtlanmıştır. Burada, farklı kompozisyona sahip CdSe/$CdSe_{1-x}Te_x$/CdSe/CdS ($0,3 \leq x \leq 0,6$) tip-II nanolevhalarının kullanılmasıyla üretilen IGY'ler gösterilmiştir. En iyi performanslı üretilen LGY, %7,29 optik güç dönüşüm verimliliğiyle bugüne kadar nanolevhalar için raporlanan en yüksek değere sahiptir. Tip-II nanolevhalar ölçeklenebilirlikleri ve uygun maliyetleri nedeniyle tarım için seralarda, bina cephelerinde, havacılık ile uydu ve uzay araçlarının güneş panellerinde olmak üzere farklı IGY uygulama alanlarında büyük potansiyel taşımaktadır.

Anahtar sözcükler: Koloidal yarıiletken nanokristaller, nanolevhalar, tip-II bant hizalaması, ışıyan güneş yoğunlaştırıcı, tümleşik fotovoltaikler.

Acknowledgement

I would like to express my deepest gratitude to my advisor, Prof. Hilmi Volkan Demir, whose expertise, guidance, and vision have been instrumental throughout this research. His discipline and dedication always inspired me. I am genuinely grateful for the opportunity to learn and grow under his supervision.

I would also like to thank my jury members Assoc. Prof. Yegân Erdem and Assist. Prof. Yusuf Keleştemur for their valuable time and consideration of my thesis.

“No one can whistle a symphony. It takes a whole orchestra to play it.”: Demir Group has always shown me the power of supporting each other and team spirit. I would like to thank group members who have built this spirit from past to present:

Özgün Akyüz, Emre Ünal, Dr. Aysan Khaligh Vazirabadi, Hamed Dehghanpour Baruj, Rumon Miah, Mohsin Waris, Taha Haddadifiam, Ahmet Tarık Işık, İklim Bozkaya, Taylan Bozkaya, Anıl Çağrı Atak, Furkan Şahin, Tuğba Kılıç, Dr. Farzan Shabani, Dr. Tatiana Lastovina, Dr. Mojtaba Sadeghi, Dr. Zahra Adelpour, Dr. Andriy Budnyk, Dr. Nina Sheremet, Dr. Volodymyr Sheremet, Muhammad Ahmad, Rabia Önen, Dr. Zeynep Dikmen, Dr. Satish Kumar, Dr. Fırat Karaboğa, Yavuz Selim Aydın, Alkım Gökbayrak, Tunç Bektaş.

I would like to thank the technical and administrative personnel at UNAM, especially for the kindness of Duygu Kazancı and Ayşegül Torun.

I would like to give special thanks to Dr. Savaş Delikanlı, who contributed not only my scientific growth but also my personal growth. As he always tells and reminds us, life has ups and downs...

I am sincerely grateful to Dr. Betül Canımkurbey, from the first day of my journey she has been a part of my life. It is hard to describe the meaning of her to me, but I made a lifelong friendship that only happens once in a blue moon.

My dear friend Furkan Işık, I cannot remember a single ordinary memory involving you and me (Europe trip – let’s not forget it). Thank you for always being by my side on good and challenging days, and cheers to creating many more new memories.

My chosen family, Yağmur, Beste, Dilan, and Sercan, thank you for always listening to and motivating me during this period. Your "Go girl!" was always in my head <3

From the bottom of my heart, I would like to thank my mother Nuray, my father Ertekin, and my brother Kaan for their endless and unconditional support. My precious family, who made me who I am today and always motivated me to follow my passion, I can never repay you.

My last and big thank you to the one who always holds my hand, Efe. I am so lucky to have you accompany me on this journey.

Contents

List of Figures

Chapter 1

Introduction

Increasing worldwide energy demand and global warming have intensified interest in renewable and sustainable energy research [1]. Due to the fact that solar energy offers abundant and clean energy, it should not be surprising to find a solution in this direction. Still, an enormous amount of effort must be made to convert sunlight into electrical power effectively.

In the late 1970s, the operating principle of luminescent solar concentrator (LSC) was introduced by Adolf Goetzberger and Volker Wittwer [2]. The main idea of the working system is to collect and guide sunlight into a small area where it is integrated with photovoltaic cells and then converted to electricity. Since re-emitting and guiding of light in LSC originates from luminescent species, various materials have been worked on, such as organic dyes, rare-earth ions, and colloidal semiconductors [3].

Since organic dyes have a high quantum yield and are also easily soluble in polymer matrices, they have been the initial and most extensively investigated luminophores for LSC applications. However, due to their typical narrow absorption band in the UV and visible regions of the spectrum, organic dyes can only convert a small amount of the solar spectrum. The emission spectrum of organic dyes in the visible range causes spectral mismatch and thermalization losses due to band gap energy difference with silicon. Large-scale, efficient device development is limited by extensive spectrum overlap, which is the root cause of reabsorption losses. Chemical composition is the main reason for ineffective devices. The photoluminescence yield will be reduced due to spectrum coverage issue since the major absorption band depends on the chain length, making the dye structure unstable.

Luminescent rare earth ions are also promising candidates for luminophores in LSCs owing to wide absorption and narrow emission spectrum, photostability, and high quantum yield; nevertheless, low absorption is a limitation of the whole procedure. Even though rare earth ions have many intriguing properties, their limited thermal and photochemical stability and photodegradation from UV light significantly hinder their practical applications.

Another excellent material as a luminophore for LSCs is colloidal semiconductor nanocrystals (NCs). They draw attention of the scientific community because of the ability to easily alter their optoelectronic properties via tailoring their size, shape, composition, and surface ligands [4]. Changing the size scale from a few hundred to a few thousand atoms affects quantum confinement and is essential because it separates energy levels between electronic states [5]. Moreover, the surface-to-volume ratio rises dramatically with decreasing nanocrystal size, making the nanocrystal effortlessly dispersible in solvents. Dispersibility of colloidal nanocrystals in various non-polar and polar solvents through control of their surface bound ligands and possibility of embedding them easily into the different matrixes makes them unique candidates for LSCs as luminophores [6].

The engineering of optical properties is also possible with heterostructures besides traditional methods such as changing size and composition. The abovementioned high surface-to-bulk ratio of NCs has higher surface atoms compared to bulk materials with unsaturated dangling surface orbitals. These unstable bonds reduce the optical features by attracting electron or hole capturing with electrical charge rather than generating electron-hole pair (exciton) [7]. In order to mitigate this adverse effect, carriers are prohibited from reaching the surface by ligand-capping open bonds and the overgrowth of new layers on NCs [5].

Type-I, quasi-Type-II, and Type-II are the three electronic heterostructures of NCs typically given in the literature. In the Type-I or “straddling” electronic structure, the edge energy levels of the valence and conduction bands of the core material have positions inside the band gap of the shell material, which leads to localization of the carriers spatially in the same layer, which is generally the core layer [8]. The band structure of the quasi-type-II electronic heterostructure is highly similar to that of type-I, with the exception that type-I has a significantly larger band offset for the conduction band [9]. The electron exhibits a wavefunction distribution in all domains, whereas the hole exists in the core. The NCs' emission and absorption spectra are redshifted due to this loosened confinement on the electron, which is adjustable by changing the shell size [9]. On the other hand, the "staggered" or type-II electronic structure allows for the recombination of charge carriers at the core/shell interface or their spatial separation to the core and shell regions, respectively, by placing one of the core material's band edges in the gap of the shell material [8].

Type II materials are extremely promising for near-infrared (NIR) emission because the radiative recombination of the spatially indirect exciton will have lower emission energies than shell and core material [3]. For the fabrication of LSCs, emission around NIR is crucial primarily for two reasons. The first concern is the spread of energy in the solar spectrum. The majority of the luminophores typically absorb light below 500 nm, limiting absorption to the ultraviolet and visible regions of the spectrum, resulting in around 60% of solar energy unabsorbed [3]. Finding the ideal spectral match for the solar cell is equally crucial. Luminophores emitting in the near-infrared region fit perfectly with the 400-1000 nm operating range for Si solar cells, which is used in many applications [3]. In addition, Stoke's shift in type-II materials as a result of spatially indirect recombination is a key for obtaining high-efficiency LSCs owing to the suppression of reabsorption losses in the device.

In this thesis, we focus on enhancing the efficiency of LSC benefiting from the type-II nanocrystal. We will investigate it in three main parts: The first is the synthesis of type-II core/crown nanoplatelets (NPLs) emitting close to NIR, and the second is the fabrication of LSC with type-II core/crown NPLs. Finally, the measurement results will be shown and evaluated carefully.

Chapter 2

Colloidal Semiconductor Nanocrystals

Analyzing crystallites within the nanoscale has opened up new perspectives in the semiconductor material world. Although over 30 years has passed since the first synthesis of colloidal nanocrystals [10], the ability to tailor size and shape composition according to desired optical and electronic features still excites many researchers and engineers. The most crucial effect originates from the quantum confinement of the dimensions changing between 2-20 nm.

In this chapter, we will analyze the synthesis and application perspective of nanoplatelets. Due to nanoplatelets giving a chance to change size, lateral shape, composition and structure, it is a promising candidate for applications such as light-emitting diode (LED), laser, luminescent solar concentrator (LSC) and biomedical applications.

2.1. Basic Concepts of Semiconductor Nanocrystals

Semiconductor nanocrystals are tiny particles showing size-dependent optical and electrical characteristics. The band structure arises when hundreds to thousands of atoms quantum mechanically couple with one another [11]. The band gap can be tuned by adjusting the crystal's physical size and shape. While energy levels continue for the valance and conduction band of bulk semiconductors with specific band gaps, colloidal semiconductors have discretized energy levels with expandable band gaps. This salient phenomenon results from the quantum confinement effect [11] which offers precise control over the NCs.

The quantum confinement effect appears once the particle size nears or falls below the Bohr exciton radius [12], α_B, which is given by:

$$a_B = \frac{\varepsilon_0 \varepsilon h^2}{\pi e^2 \mu} \tag{2.1}$$

where ε and ε_0 are the relative permittivity of the semiconductor and the permittivity of the free vacuum, respectively; μ is the reduced mass of the electron and hole; and e is the electron charge.

Photoexcitation is a mechanism for the generation of electron-hole pair (exciton) as a result of absorbing a photon of higher energy than the band gap. Exciton exists above the energy levels due to energy difference between the incident photon and band gap; the excessive energy spreads out as heat, and the electron and hole move to the band edge [13]. Recombination of electron-hole pair creates a photon with an energy of bandgap. These are the main reasons for the optical absorption and emission of NCs. In addition to the actual size of inorganic core, organic (and inorganic) ligands enable chemical and colloidal stability, and the polarity level of the ligands specifies the solvent, either polar or non-polar.

2.2. Colloidal Synthesis of Semiconductor Nanocrystals

Colloidal nanocrystal synthesis, a sub-branch of synthetic chemistry, has shown great development in the last decade due to the aforementioned possibility of finely tuning the size (2-20 nm), controlling the shape along various dimensions (quantum dot, quantum wire, quantum well), tailoring composition (III–V and II-VI group of elements) and adapting heterostructures (type-I, quasi type-II and type-II), which are essential for optoelectronic applications.

The procedure of colloidal synthesis typically consists of multiple sequential steps: Starting with a homogeneous solution, growing prepared nuclei, size-separation of particles from the reaction mixture, and postpreparative treatments [11]. This prerequisite is fulfilled either by the hot-injection technique, in which the precursors are quickly injected into a hot solution and then allowed to cool, or by heating the reaction mixture continuously, which can also help separate the nucleation and growth parts.

The nucleation and growth of NCs occur in the solution phase, facilitated by organic surfactant molecules that attach to the crystal surfaces as they grow. Typical surfactants employed include long-chain carboxylic acids, phosphonic acids (such as oleic acid and n-octadecylphosphonic acid), alkanethiols (like dodecanethiol), alkylphosphines, alkylphosphine oxides (notably trioctylphosphine (TOP) and trioctylphosphine oxide (TOPO)), and alkylamines such as hexadecylamine. These surfactants play a critical role in adjusting the kinetics of nucleation and growth, which must be meticulously balanced. An imbalance, where nucleation occurs too slowly or quickly relative to growth, can result in either bulk crystal formation or molecular clusters. It is

challenging to achieve dynamic equilibrium, but it can be handled empirically by optimizing the mixture of molecular precursors, surfactants, solvents, and reaction parameters, including reaction temperature and time. In many cases, annealing out crystalline lattice imperfections and forming highly crystalline particles requires temperatures as high as 300 °C [11].

The LaMer model, seen in Figure 2.1a, is a well-known model for identifying the nucleation and growth scheme of the NCs [14]. According to the fundamental interpretation, small crystallites naturally and uniformly nucleate in the solution as the concentration of free monomers increases and the solution becomes supersaturated. After completing this nucleation step, the nanocrystals proceed through a growth stage when additional monomers bond to the surface and free monomers nucleate on the small crystallites' surface, expanding the size of the NCs.

The thermodynamic equilibrium controlling the system's total energy is the underlying reason behind the NCs' nucleation and growth. Identifying the spherical cluster's Gibbs free energy as

$$\Delta G = -\frac{4}{3}\pi r^3|\Delta G_v| + 4\pi r^2\gamma \tag{2.2}$$

where γ is the surface energy per unit area, r is the sphere's radius and ΔG_v is the Gibbs free energy per unit volume. Beyond a certain radius, the Gibbs free energy begins to diminish. Although the equation's first part is negative, which drives the generation of larger spheres, the second term is positive since the surface area increases as the sphere becomes larger (Figure 2.1b).

Despite the LaMer model's isotropic growth scheme providing a clear understanding of the colloidal synthesis of NCs, it cannot explain the anisotropic development of NCs. The anisotropy in the shape results from the energy differential between the various facets, which promotes the growth of some planes relative to the other facets and leads to the anisotropic expansion of the NCs. Slow-growing facets become apparent, whereas fast-growing facets keep expanding.

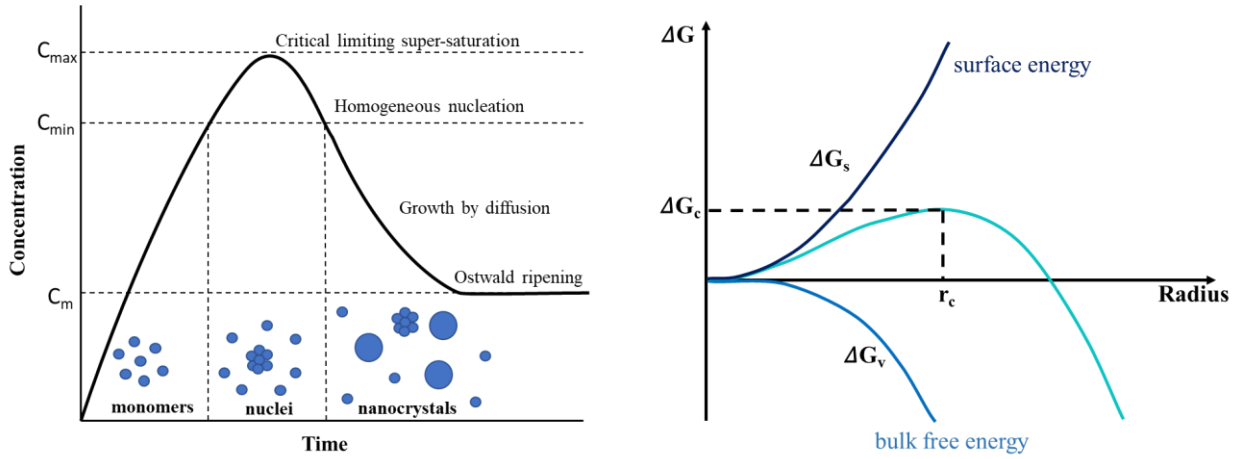

Figure 2.1. a) The LaMer growth model illustrated schematically by three fundamental stages: At the initial stage, increasing the concentration of monomers elevates the system to a level of supersaturation, approaching the phase where homogeneous nucleation occurs. During the second stage the concentration of the free monomers decreases when small crystallites begin to spontaneously nucleate in the solution. The final stage involves the inhomogeneous nucleation and growth of the small nuclei, which results in an increase in the dimensions of the NCs and a fall in the concentration of free monomers. Ostwald ripening occurs at this phase as well, where one crystal dissolves in the solution to facilitate the growth of another crystal. b) The Gibbs free energy, along with the surface and volume terms, influence the system's total energy. As the dimension of the NCs increases, the volume energy per unit volume decreases, and the surface energy per unit area declines. The Gibbs free energy begins also to decline at a critical sphere radius (r_c).

2.3. Electronic Heterostructures of Colloidal Nanocrystals

The study of colloidal nanocrystal electronic heterostructures is a rapidly developing area in synthetic chemistry, recognized by manipulation of band gaps, charge carrier dynamics, photoluminescence features, and the like an essential part of next-generation breakthroughs in photovoltaics, optoelectronics, and quantum computing. Type-I, quasi-type-II and type-II heterostructures, which are formed by integrating several semiconductor materials together at the nanoscale, have remarkable optical and electrical properties because of interfacial phenomena and quantum confinement effects. In addition to the traditional tuning tools, (the size, shape and

composition), electronic heterostructures will be examined in detail and demonstrated in Figure 2.2.

In type-I heterostructure, the core (first component) is embedded into the second component, which has a deeper conduction and valance band [15]. This nested structure restricts holes and electrons to the core. The second component surrounds and passivates defects of the core and enhances photoluminescence quantum yield for greater efficiency in photoemission based devices [16]. The electronic structure of the inverted type-I heterostructure is the same, but the components' alignment is reversed.

The band structure of the quasi-type-II electronic heterostructure is quite comparable to that of type-I, with the exception that type-I has a significantly larger band offset for the conduction band [17]. In addition to being capable of passivating the NCs' surface, this electronic heterostructure is an excellent tool for shifting the NCs' emission wavelength [9]. The electron has a wavefunction distribution throughout all the components, whereas the hole is mostly located in the core. The NCs' emission and absorption spectra are redshifted as a result of this weak confinement on the electron, which is controllable by changing the shell's size [9].

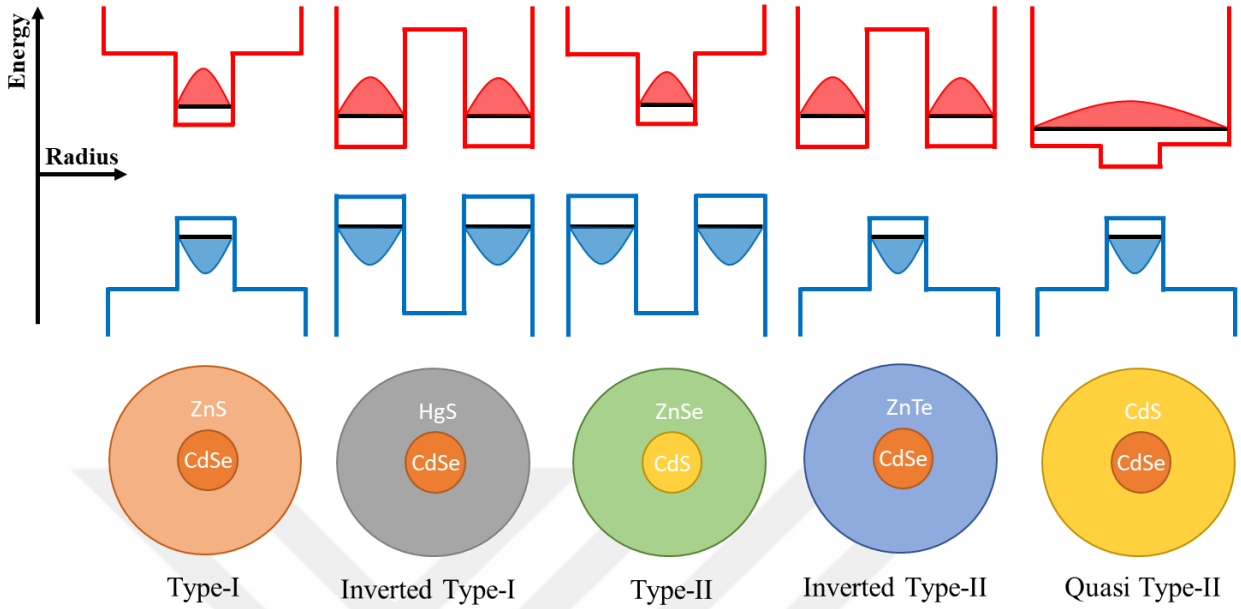

Figure 2.2. Various types of band alignment in core/shell colloidal nanocrystals. The bulk materials' valence band is shown in blue, the conduction band in red, and the confined levels in black. The ground state wavefunctions for electrons and holes are represented in red and blue, respectively.

On the other hand, type-II heterostructures are composed of materials with offset valence and conduction band edges, referring to the fact that one component's edges are at a greater energy than the second. Regardless of the material used as the light absorber, electrons will localize to the lowest energy conduction band and holes to the highest energy valence band. This offset band alignment allows charge carrier separation across the heterojunction interface easier [16]. In type-II heterostructures, excitons recombine in nanosecond time intervals, slower than comparable single material systems, which makes them appropriate candidates for catalytic and solar energy harvesting applications for the extraction of electrons [16]. Emission at low photon energies can be successfully achieved using type-II band alignment, as mentioned, making it suitable for LSC. Moreover, Auger recombination is suppressed due to the physical separation of the photogenerated electron and hole [16]. For the inverted type-II heterostructures, the first and second components change their position.

2.3.1. Nanoplatelets with Type-II Heterostructure

Colloidal two-dimensional (2D) nanoplatelets are a group of nanocrystals that grow either in the confined direction (core/shell) or perpendicular to the confined direction (core/crown) [18]. Much research has gone into developing 2D heterostructures since their debut in the late 2000's. The objectives associated with these heterostructures are to reduce the inhomogeneous widening while keeping the PL narrowness or governed cutoff wavelength.

Due to the fact that CdSe core synthesis is well established and the electrical and optical properties are understood deeply, it opens the door of different heterostructures slightly. The change in crown material results in new energy band alignments in nanoplatelets. For example, CdSe/CdS core/crown NPLs possess type-I heterostructure [19], [20], whereas CdSe/CdTe core/crown NPLs exhibit type-II heterostructure [21], [22], [23], [24].

In this thesis, we will investigate core/crown geometry. This heterostructure provides several potential benefits: (i) a novel 2D geometry that allows for band-gap engineering, (ii) large cross-sections that can be tuned separately for each material, and (iii) three recombination routes for the exciton, which can recombine across the interface, within the core, or in the crown [18]. It is also possible to change the crown structure by adapting multiple or alloying [25], [26]. While the double-crowned NPLs like CdSe/CdTe/CdSe show bicolor power-tunable emission, the alloyed crown NPLs like CdSe/$CdSe_{1-x}Te_x$/CdS demonstrate ultralow amplified spontaneous emission, increased photostability, and decreased aggregation [27],[25]. These alloyed core/crown NPLs providing enhanced PLQY and slower Auger recombination are remarkable for optoelectronic applications [28], [29],[30].

2.4. Optoelectronic Applications of Colloidal Nanoplatelets

Recently, there has been significant interest in solution-processed, atomically precise, thickness-controlled two-dimensional colloidal semiconductor NPLs thanks to their tailor-made electrical structure for optical devices [31]. 2D NPLs have a large absorption cross-section, high exciton binding energy, and giant oscillator strength due to their strong one-dimensional (1D) quantum confinement.

For high-efficiency light-emitting diode applications, the large exciton binding energy and narrow emission band are advantageous. A high optical gain is crucial for spontaneous emission with a low threshold, and one of the reasons for this property is the large absorption cross-section of NPLs. 2D NPLs have a larger capacity for charge storage and quick charge transfer so that their broad surface area makes them suitable for photocatalysis and sensing applications [31].

On the other hand, because of their excellent emission, great stability, and configurable optoelectronic characteristics, which lower their reabsorption losses, colloidal NPLs have become appealing luminophores for LSCs [32]. The effective down-conversion and propagation of photons along the waveguide's edge are critical to the functioning of LSCs. This criterion unravels with the usage of NCs having large Stokes shift in order to limit reabsorption. Moreover, NPLs are also remarkable luminophores owing to their high photoluminescence quantum yield (PLQY) value (>95%), having an effect on emitting light through photoluminescence or losing energy as heat [26], [33].

2.4.1. Luminescent Solar Concentration of Colloidal Nanocrystals

Luminescent solar concentrator uses photon absorption, luminescence, and waveguiding mechanisms to collect and concentrate photons from the sunlight. The LSC device is composed of a planar waveguide with photovoltaics (PVs) deployed at the waveguide edges and embedded luminophores, as represented in Figure 2.3. Photovoltaic systems convert waveguided photons into electrical energy. The process of collecting photons from a large area and concentrating them onto a smaller photovoltaic surface enhances efficiency and reduces the overall cost of solar energy production [34].

LSC applications encompass a variety of uses, such as integrating solar collectors into smart windows, electronic devices, and fiber optics. Additionally, LSCs facilitate photon transport for passive daylighting and serve as active color filters in tandem photovoltaic cells and greenhouse panels [34].

LSCs fundamentally depend on photon transport over a centimeter scale making them vulnerable to various loss mechanisms. Approximately 75% of emitted photons are effectively trapped within a waveguide, while the remaining photons escape according to Snell’s law. However, photons

captured through total internal reflection can still be lost due to scattering from the waveguide surface, internal defects, or the luminophores themselves. Reabsorption by the luminophores can lead to nonradiative decay or emission into the escape cone. Reabsorption losses represent a significant barrier to the large-scale production and commercialization of luminescent solar concentrators [34].

According to the previous reports in literature, NCs could potentially be able to address the reabsorption issue [35], [36], [37]. The formation of NC heterostructures, which surround wider-gap semiconductors onto the smaller cores with a narrower bandgap, is one approach to overcome self-absorption. As examples, CdSe/CdS core/shell and CdSe/CdSe dot-in-rod NCs depicted in Figure 2.4 can be used in LSCs [38]. The wider-gap material controls the absorption spectra in these NCs, and red-shifted luminescence arises from either the core or via a spatially indirect transition through the heterointerface.

Another approach uses doped semiconductor NCs (e.g., ZnSe:Mn, CdSe:Cu) as luminophores in LSCs [34], [37], [38]. These nanocrystals exhibit high quantum yield and a broad Stokes shift, which minimizes or eliminates reabsorption losses in the device [34]. The synthesis of copper-doped zero-dimensional (0D) and one-dimensional (1D) colloidal semiconductor nanocrystals has garnered significant attention due to their adjustable photoluminescence (PL) emission, which can be tuned by size and composition, nearly zero self-absorption, and p-type conductivity [39]. Although Cu-doped CdSe and $CuInS_2$/CdS colloidal quantum dots (CQDs) demonstrate superior performance compared to other colloidal nanocrystal heterostructures, their photoluminescence quantum efficiency (PLQE) remains relatively low, reaching only approximately 40% [40]. Therefore, efforts should be directed towards increasing this value.

On the other hand, NPLs have received substantial attention owing to their finite vertical thicknesses. Significantly larger linear and nonlinear absorption cross-sections [41-42], suppressed inhomogeneous emission broading, giant oscillator strengths [43], and narrow spontaneous emission spectra are among the most remarkable optical features of 1D confinement over CQDs. This 1D confinement leads to a sharp step-like absorption pattern in NPLs. Thus, obtaining luminophores with extremely low absorption in the emission area, together with Stokes-shifted and step-like absorption patterns, is critical to making ideal LSCs [44]. Recent studies have shown that reabsorption in doped CQDs and CdSe/CdS heterostructures, resulting from partial overlap between optical absorption and emission spectra, significantly impair their effectiveness in large-

scale LSCs [34]. Consequently, the distinctive step-like optical absorption pattern of NPLs presents a promising solution for achieving superior LSCs. It is also essential to optimize their other critical parameters to realize the full potential of ideal LSCs.

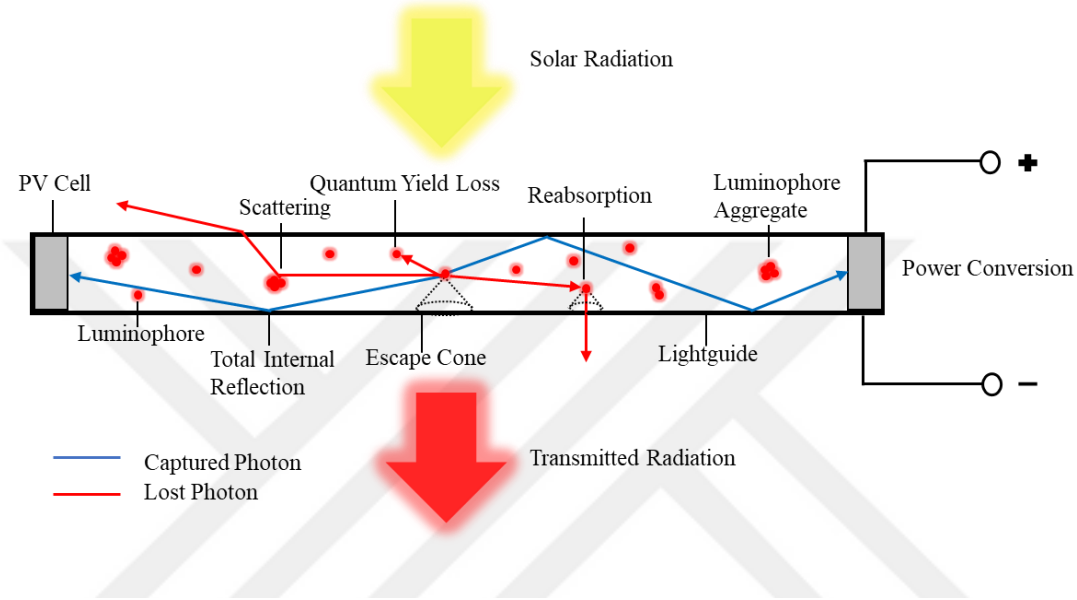

Figure 2. 3. Schematic demonstrating the processes associated with photon capture and loss in an LSC integrated with PV.

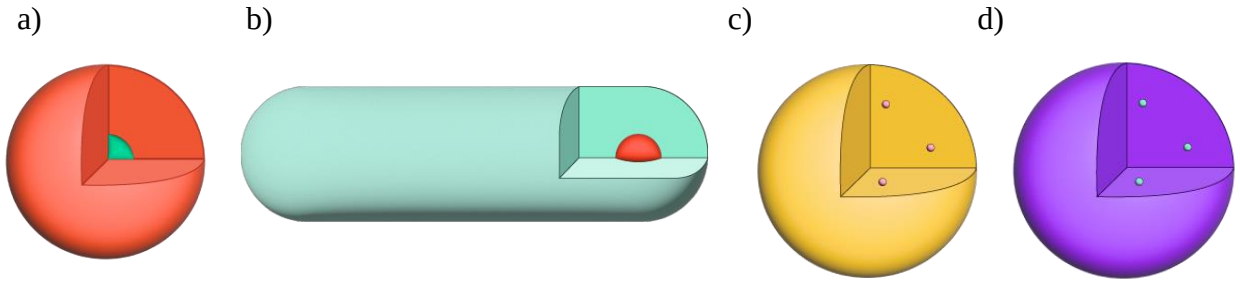

Figure 2.4. Schematics showing the four distinct types of nanocrystals suggested for usage as a luminophore in LSCs: a) CdSe/CdS core/shell, b) CdSe/CdS dot-in-rod, c) $Zn_{1-x}Mn_xSe$, and d) $Cd_{1-x}Cu_xSe$ NCs.

Chapter 3

Synthesis and Characterization of CdSe/CdSeTe/CdSe/CdS Core/Multicrown Type-II Nanoplatelets

Colloidal semiconductor quantum wells, commonly referred to as nanoplatelets (NPLs), are atomically flat and quasi two-dimensional materials. Their lateral dimensions exceed the exciton Bohr radius, while quantum confinement arises from their atomic-scale vertical thickness, typically consisting of a few monolayers (3 ML, 4 ML, 5 ML). NPLs exhibit remarkable optical features, including narrow luminescence spectra (~ 12 nm), sharp step-like absorption profiles, giant oscillator strength, and greatly large linear and nonlinear absorption cross-sections [42]. These features make NPLs excellent candidates for designing and fabricating heterostructures and optoelectronic devices.

As mentioned in Section 2.3, in type-II heterostructures, excitons recombine in nanosecond timescale, which is slower compared to that of single-material systems. This slower recombination makes them suitable candidates for catalytic applications and solar energy harvesting, particularly for luminescent solar concentrators (LSCs). Furthermore, the emission at low energies and the suppression of Auger recombination are additional outstanding features for those interested in exploring these relatively uninvestigated type-II heterostructures.

CdSe/CdTe core/crown type-II NPLs were synthesized by Kelestemur et al. [45] with a well-controlled CdTe crown layer, reaching a PL-QY of 40-50%. CdSe/CdTe core/crown NPLs show increasingly red-shifted photoluminescence arising from the intermediate transition across the core/crown interface, with the increasing width of the CdTe crown layer. Furthermore, they show notably high elongation in radiative lifetime because of spatially distinct excitons produced at the type-II interface. However, CdSe/CdTe core/crown NPLs exhibit limited optical tunability due to quantum confinement occurring only in the vertical direction. With the growth of the CdTe crown layer, emission can be tuned within 620-660 nm, and after that, PL-QY decreases sharply. Therefore, novel hetero-NPL architectures should be developed for high performance.

To meet this requirement, CdSe/$CdSe_{1-x}Te_x$ NPLs were synthesized with various compositions of Te from x=1.00 to x=0.02 for tuning excitonic properties [46]. The results of this study indicate

that a rise in the concentration of Te in the crown layer red-shift the emission peak wavelength and elongates radiative fluorescence lifetimes. In addition, CdSe/$CdSe_{1-x}Te_x$ core/crown NPLs exhibit significantly better PL-QY (up to 95%) due to ultrafast localization of the photogenerated holes around Te atoms and their radiative recombination in the nanosecond time interval. On the other hand, despite their extraordinary features, these NPLs are unstable in solution and form gels, which makes them complicated to employ in potential applications. To address this problem, Dede et al. demonstrated a second crown consisting of CdS around the periphery of CdSe/$CdSe_{1-x}Te_x$ core/alloyed-crown structures [47]. The CdS band offset is positioned at higher energies in comparison to the $CdSe_{1-x}Te_x$ band offset, which preserves the emission features and extends the absorption cross-section.

A lattice mismatch of approximately 10% occurs between the CdTe and CdS crown layers, resulting in the development of nonradiative defect sites. The CdS crown layer grows on the corner of NPLs and further promotes nonradiative recombination, which is disadvantageous for light-emitting devices. The growth of CdSe crown between the CdSeTe and CdS crowns reduces the lattice mismatch and promotes uniform growth of CdS around the NPLs. The lattice mismatch between CdSe and CdS is ~ 5%, considerably lower compared to CdTe and CdS. Thus, the tailoring of CdSe crown between the $CdSe_{1-x}Te_x$ and CdS crowns mitigates the lattice mismatch and strain, resulting in superior properties such as near-unity quantum yield, high Stokes shift, and stability in nonpolar solvents.

In this chapter, the synthesis of luminophore used for the fabrication of LSC will be detailed with structural and optical characterizations.

3.1. Synthesis of CdSe/CdSeTe/CdSe/CdS Core/Multicrown Type-II Nanoplatelets

A precise multi-step methodology has been applied in synthesizing CdSe/CdSeTe/CdSe/CdS core/multicrown type-II NPLs to establish complete control over the resulting properties. Seed-mediated growth was used to synthesize CdSe/CdSeTe/CdSe/CdS core/multicrown NPLs. The synthesis of 4 ML CdSe core NPLs is the first step in this procedure. The CdSeTe, CdSe, and CdS

crown layers are grown subsequently controlling temperature and using regulated precursor solution injections with sufficient time intervals ensuring uniform growth.

Chemicals

Sodium myristate, cadmium acetate dihydrate, cadmium nitrate tetrahydrate ($Cd(NO_3)_2.4H_2O$), trioctylphosphine (TOP), sulfur (S), selenium (Se), tellerium (Te), octadecene (ODE), oleic acid (OA), ethanol, hexane, and acetone were purchased from Sigma Aldrich.

Cadmium Myristate

In this thesis, NPLs are employed in the form of CdSe/CdSeTe/CdSe/CdS core/multicrown structures. The main substance of core synthesis is Cd(myr), which was synthesized with slight modifications to the method previously described by Altintas et al. [48]. Specifically, 2.46 g of cadmium nitrate was dissolved in 80 mL of methanol and 6.26 g of sodium myristate in 500 mL of methanol. These solutions were put together and stirred for 5 h. The resulting mixture was then precipitated by centrifugation and washed twice with methanol. The final white product was dried under a vacuum at room temperature overnight. The synthesized Cd(myr) was subsequently stored in a refrigerator at approximately 4 °C.

Colloidal Synthesis of 4 ML CdSe Core Nanoplatelets

4 ML CdSe NPLs were grown to be used as seeds. The 4 ML CdSe NPLs synthesis followed an established protocol [49]. In a three-neck flask, 170 mg of cadmium myristate, 12 mg of selenium (Se), and 15 mL of octadecene (ODE) were loaded and subjected to vacuum degassing for one hour at room temperature. Subsequently, the mixture was heated to 240 °C under an inert environment. Upon reaching 195 °C, 80 mg of cadmium acetate dihydrate was introduced. After one minute of keeping the reaction at 240 °C, 0.5 mL of oleic acid was injected. Finally, NPLs were separated from the byproducts by selective precipitation employing acetone as an anti-solvent and hexane as a solvent after the process had gradually cooled to ambient temperature.

Synthesis of 4 ML CdSe/$CdSe_{1-x}Te_x$/CdSe/CdS Core/Multicrown Nanoplatelets

A three-neck flask was filled with 30 mL of ODE and 4 ML of CdSe NPLs dissolved in hexane. Hexane was removed from the reaction mixture by degassing it for one hour at room temperature while under vacuum. After injecting 1.5 mL of the anisotropic growth mixture while the nitrogen flow was running, the solution proceeded to degas for another one hour. Following this step, the

temperature was increased to 220 °C in an environment of nitrogen. The 0.03 M TOP-$Se_{1-x}Te_x$ in ODE was injected at 25 mL/h after preparation in a glovebox with a nitrogen environment. While injection was continuing, 1 mL of anisotropic growth mixture was injected. After the 6 mL injection was completed, the mixture was waited for 5 min before proceeding with the subsequent CdSe crown growth. After that, 0.03 M TOP-Se in ODE was injected at 25 mL/h. During this injection, 1 mL of the anisotropic growth mixture was also introduced. After 4 mL of the total injection, the mixture was again waited for 5 min before the subsequent CdS crown growth. The final crown layer was grown by injecting 0.15 M ODE-S at a rate of 8 mL/h. The reaction was then quenched with a water bath, and the nanoplatelets were isolated from unwanted species through selective precipitation, using hexane as the solvent and ethanol as the anti-solvent. The particles were redispersed and stored in hexane. The growth of each crown layer could be distinctly monitored by the characteristic peaks corresponding to the different elemental compositions in the absorption spectra.

3.2. Structural Characterization of CdSe/CdSeTe/CdSe/CdS Core/Multicrown Type-II Nanoplatelets

Structural characterization methods include X-ray diffraction (XRD) and transmission electron microscopy (TEM). The crystal structure, orientation, defects, and strain are among the physical characteristics that can be analyzed using XRD [50]. Moreover, to examine the morphology of the nanocrystals and identify the particle size distribution, TEM images are used [51]. Here, we detail these two techniques for characterizing the structural features of our NPLs.

3.2.1. X-Ray Diffraction

X-ray diffraction is a crucial tool for examining the structural properties of materials, particularly at the atomic or molecular scale. It is most effective for crystalline or partially crystalline substances, which possess periodic structural order, but it can also be applied to the study of non-crystalline materials. XRD is used to obtain crystalline phase, lattice parameters, degree of crystallinity, grain size, film composition, and film thicknesses. Since the measurement system is relatively fast, non-destructive and precise, it is a common characterization technique.

X-ray is electromagnetic radiation (light wave) with wavelengths on the order of nanometers. The interatomic lengths in crystals, ranging from 0.15 to 0.5 nm, are of the same magnitude, and diffraction of X-ray generates both constructive and destructive interference effects as shown in Fig. 3.1., where an X-ray beam, of wavelength λ, is incident at an angle, θ, onto a series of atomic planes of spacing, d [52]. The incidence angle with respect to the crystalline plane is equal to the angle, θ, at which the X-ray beam scatters the planes. The distance in Figure 3.1., shown in red, indicates the relative phase shifts between X-rays scattered off the first and second planes. Constructive interference occurs for certain angles θ_B depending on the interplanar spacing, d, and according to

$$n\lambda = 2d_{hkl} \sin \theta_B \tag{3.1}$$

Equation 3.1 is known as the Bragg equation. θ_B is referred to Bragg angle, hkl is Miller indices of the crystallographic plane, n is an integer. All XRD measurements are based on the Bragg equation, which correlates the angular position of diffracted X-rays to the lattice spacing [52].

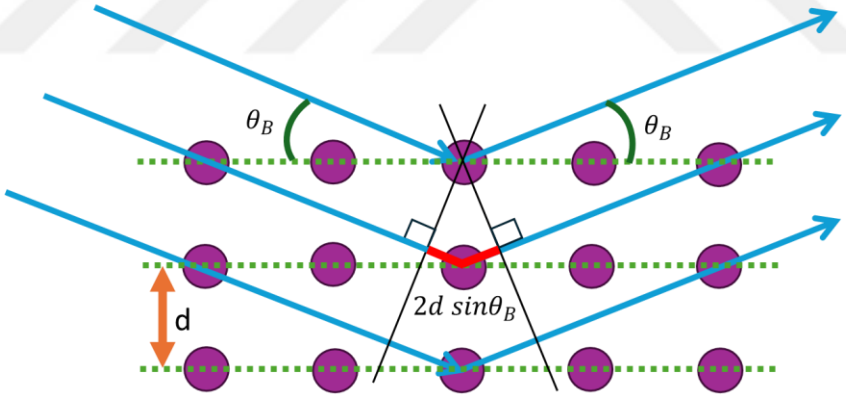

Figure 3.1. Schematic representation of X-ray scattering from crystalline planes.

The X-ray source, detector, incident (or primary beam) optics, receiving (or diffracted beam) optics, and goniometer are the five main parts of an X-ray diffractometer, as seen in Figure 3.2. X-rays can be produced with an X-ray tube, rotating anode, X-ray generator, microfocus tube, or synchrotron. Any of the systems mentioned above can create radiation, which is generally composed of rays with a range of wavelengths and directions of travel. An XRD instrument's collimation section aims to generate a relatively thin X-ray beam, has a restricted wavelength distribution, and travels in the same direction. Various types of detectors can be employed, such

as film, scintillation detectors, and more commonly, two-dimensional detectors, which offer significant advantages. When conducting a diffraction experiment using a two-dimensional detector, the sample must first be positioned in the X-ray beam so that diffracted rays hit the detector. The sample must then be exposed for a predetermined period of time. The computer subsequently reads each pixel's resultant region of intensities, typically photon counts, and displays the data as a false-color image. The goniometer, the final component, controls the angles between the source, detector, and sample surface.

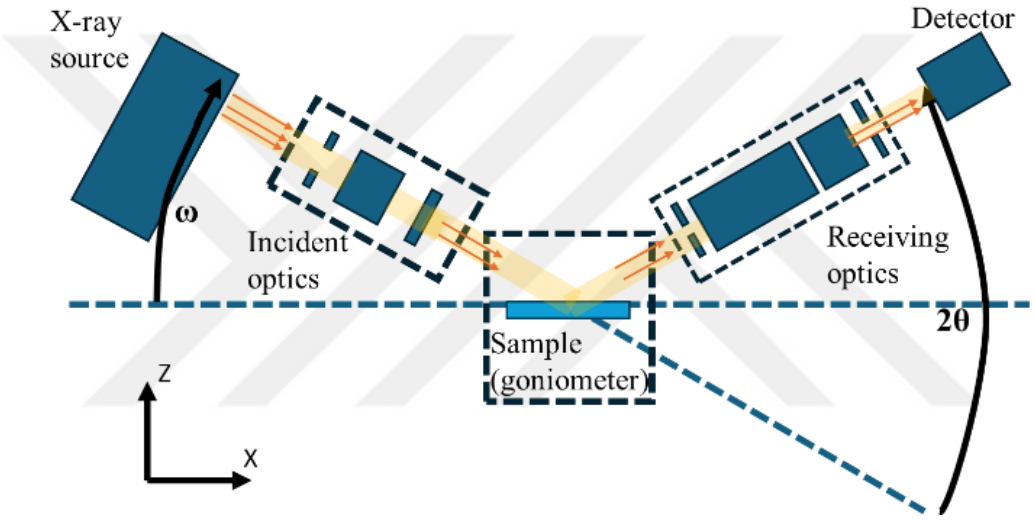

Figure 3. 2. Schematic of working principle of the XRD system.

In this thesis, an X'Pert PRO powder diffractometer (PANalytical) was utilized for measurements. The samples were prepared as thick films on quartz substrates. The results are depicted in Figure 3.3.

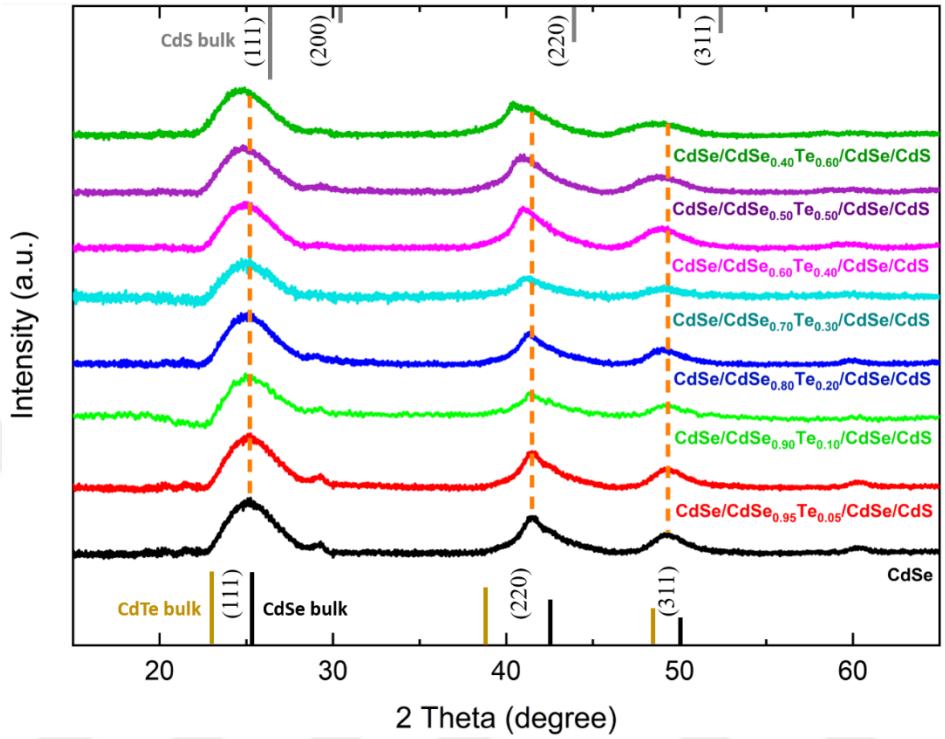

Figure 3. 3. X-ray diffraction patterns of the 4 ML CdSe core-only NPLs and the CdSe/$CdSe_{1-x}Te_x$/CdSe/CdS core/multicrown NPLs with various compositions. The black and dark yellow bars (on the bottom) and the grey bars (on the top) symbolize the diffraction peaks of the bulk CdSe, CdTe and CdS having zinc blende structure, respectively.

According to Equation 3.1, the angle, θ_B, decreases as the interplanar spacing, d, increases. It is known that interplanar spacing is proportional to the lattice constant of nanocrystal. In the literature, the lattice constants for CdTe, CdSe, and CdS are 6.56, 6.14, and 5.89 Å, respectively. As illustrated in Figure 3.3., an increase in the tellurium percentage of NPLs results in a shift toward smaller angles. Additionally, the CdSeTe peak should be located between the CdSe and CdTe peaks, corroborating the alloying of selenium and tellurium in the crown layer. The Miller indices of the observed peaks further confirm that the structure is zinc blende, consistent with the expected crystal structure.

3.2.2. Transmission Electron Microscopy

Transmission electron microscopy is a powerful instrument in the characterization of nanocrystals, providing detailed information about their structural, morphological, and compositional attributes at the atomic scale. In this thesis, TEM has been used to examine the size and shape of the NPLs we synthesized.

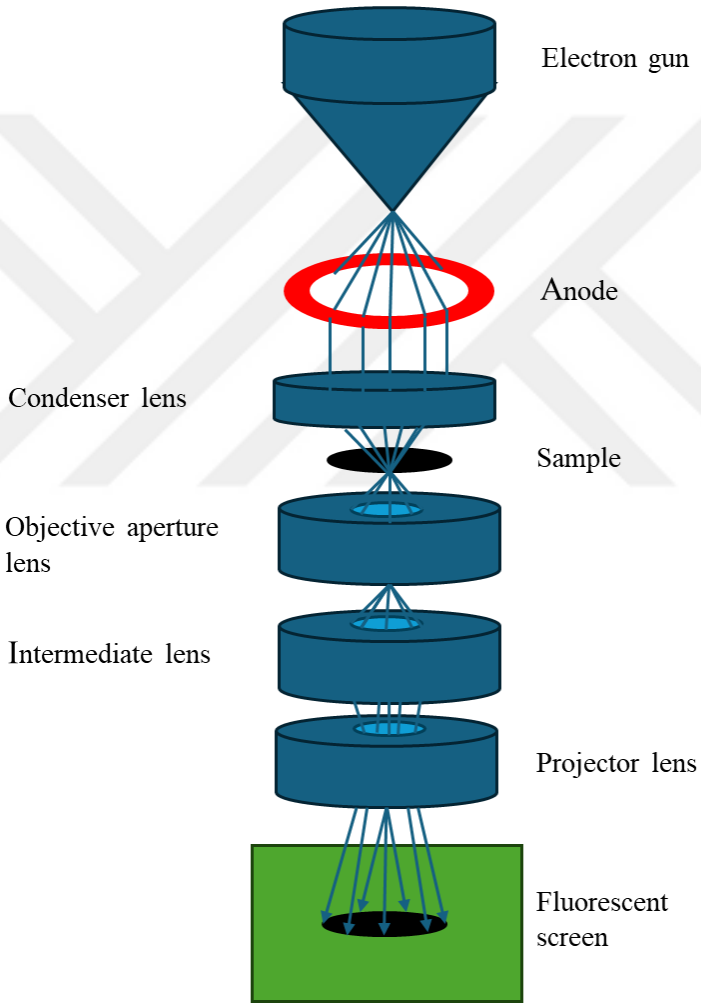

Figure 3. 4. Schematic of working principle of TEM.

As depicted in the basic schematic of TEM in Figure 3.4., electrons are generated by an electron gun, which can be either LaB6 or thermionic. They are accelerated under a high voltage, typically 100 to 300 kV. The electron beam is subsequently focused by condenser lenses composed of

magnetic coils. Upon striking the surface of a specimen, the electrons are scattered. These scattered electrons are then collected by objective lenses, resulting in the formation of an image. A high vacuum is maintained throughout the operation to keep air from absorbing electrons in the electron microscope. TEM typically achieves a resolution of 0.2 - 0.5 nm, corresponding to the typical distance between two atoms in a crystal lattice [53].

For our NPLs, TEM sample preparation is as follows. First, the solution containing NPLs is diluted. Then, this solution is cleaned many times in order to remove extra ligands that may otherwise induce a charging effect while imaging. After completing this process, 10 µL of this diluted and cleaned solution is dropped with a micropipette on a copper mesh grid, and hexane (nonpolar solvent of NPLs) is allowed to evaporate. The copper grid is placed under vacuum for further drying before being examined in a TEM.

The influence of tellurium concentration on the size and shape of synthesized NPLs is evident in Figure 3.5. The images distinctly illustrate the successful formation of uniform CdSe/CdSeTe/CdSe/CdS core/multicrown NPLs with precise geometrical shapes. The lateral dimensions of the CdSe/CdSeTe/CdSe/CdS core/crown NPLs are larger than those of core-only CdSe NPLs (7 nm) due to the lateral expansion of the CdSeTe, CdSe, and CdS crown layers. Specifically, increasing the Te concentration from 20% to 80% in the crown layer results in a 25% increase in the lateral size of the NPLs. For instance, CdSe/$CdSe_{0.2}Te_{0.8}$/CdSe/CdS NPLs exhibit lateral dimensions of 12 nm, compared to 9 nm for CdSe/$CdSe_{0.8}Te_{0.2}$/CdSe/CdS NPLs. The modification of the crown layer's composition does not significantly alter the shape of the nanoplatelets, as illustrated in Figure 3.5. Despite the increasing proportion of tellurium, the rectangular shape of the nanoplatelets is consistently maintained.

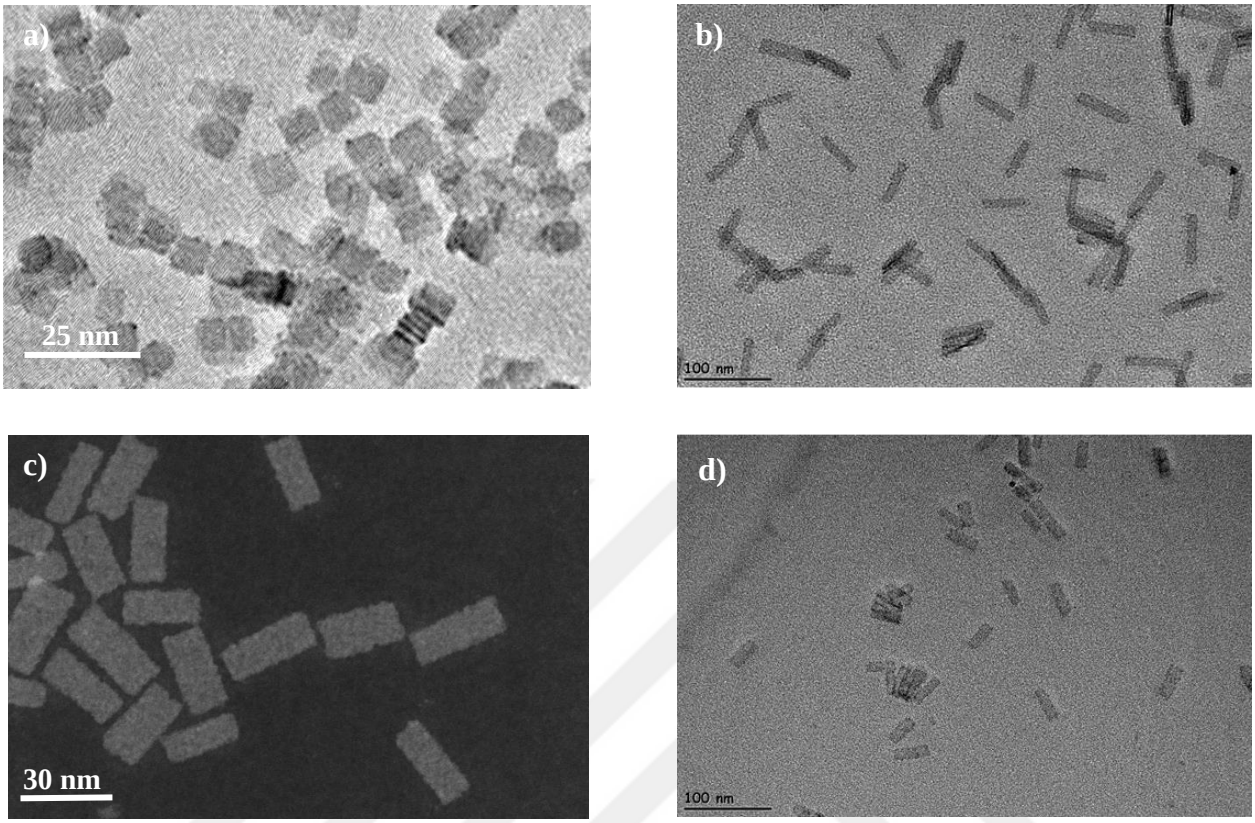

Figure 3.5. TEM images of a) 4 ML CdSe core NPLs, b) CdSe/$CdSe_{0.8}Te_{0.2}$/CdSe/CdS core/multicrown NPLs, c) CdSe/$CdSe_{0.8}Te_{0.4}$/CdSe/CdS core/multicrown NPLs, and d) CdSe/$CdSe_{0.2}Te_{0.8}$/CdSe/CdS core/multicrown NPLs.

3.3. Optical Characterization of CdSe/CdSeTe/CdSe/CdS Core/Multicrown Type-II Nanoplatelets

Absorption spectroscopy, photoluminescence spectroscopy, time-resolved fluorescence (TRF) spectroscopy, and reabsorption measurements are employed in the optical characterization of nanoplatelets due to their ability to provide a comprehensive understanding of the electronic structure and optical properties of these synthesized nanocrystals. Absorption and photoluminescence spectroscopies are used to assess the steady-state excitonic properties of the NPLs, while reabsorption and TRF measurements are invaluable for elucidating their emission kinetics. The optical characterizations were carried out using a fluorescence spectrometer (Cary

Eclipse) for PL measurements and a UV-Vis spectrometer (Cary 100) for absorption measurements. A PicoQuant FluoTime 200 spectrometer was used to measure TRF.

3.3.1. Absorption Spectroscopy

There are four prospective results of incoming light interactions with materials: absorption, transmission, reflection, or scattering. The material's absorption spectrum shows the portion of incoming light it absorbs. Our NPLs absorb a certain amount of the UV-Vis region of the electromagnetic spectrum. Characterization protocol involves placing a cuvette containing nanoplatelets dissolved in hexane within the device and scanning the UV-Vis region at all wavelengths between 300 and 800 nm. When the energy of the incoming photons exceeds the band gap, a portion of the light is absorbed, generating excitons, while the remainder is either transmitted or reflected. This absorption process can be described using the Beer-Lambert Law, as expressed in Equation 3.2.

$$A = \epsilon \times l \times C \tag{3.2}$$

where A is the absorbance (unitless), ϵ is the molar extinction coefficient (L/mol.cm) which is the material's property, l is the optical path length (width of the cuvette, cm), and C is the concentration of NPLs inside the hexane (mol/L).

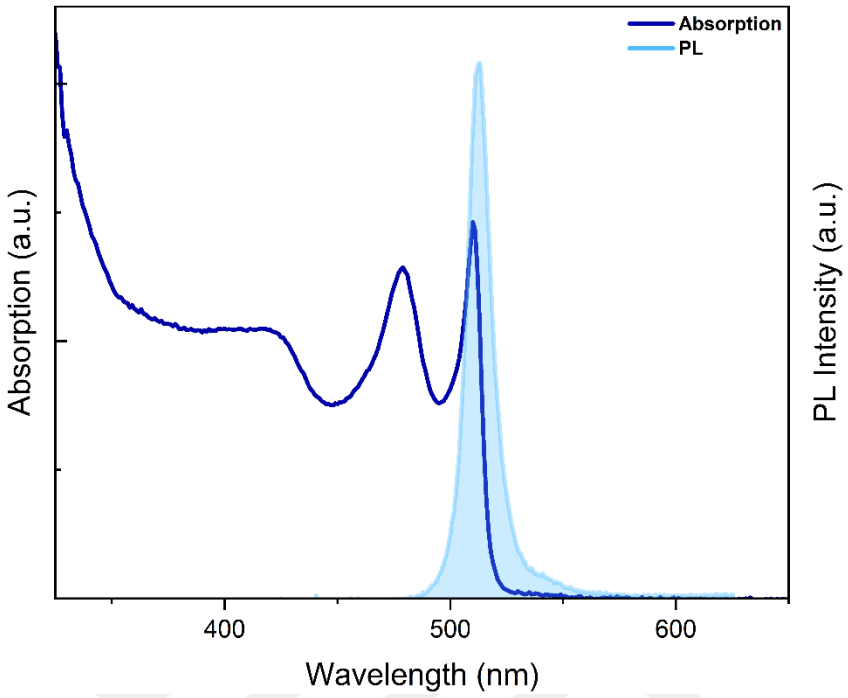

Figure 3.6. Absorption and PL spectra of 4 ML CdSe core.

As outlined in Section 2.1, the initial step is the synthesis of 4 ML CdSe core NPLs. Figure 3.6. illustrates the splitting of sharp excitonic features, including electron-light hole transitions (~ 480 nm) and electron-heavy hole transitions (~ 510 nm), indicative of the electronic structure of NPL. These NPLs are uniformly 4 ML thick, with their PL peak centered at ~ 512 nm and a full width at half maximum (FWHM) of ~ 12 nm.

Following the synthesis of the core NPLs, type-II NPLs were prepared. Absorption spectroscopy presents solid proof for the heterostructures' growth. For instance, it can be used to ensure that various crown compositions have formed in 4 ML CdSe/$CdSe_{1-x}Te_x$/CdSe/CdS NPLs. Compared to the CdSe core spectrum, the growth of the crown layers generates new peaks, as seen in Figure 3.6. Since the crown structures and the core have the same thickness, the core's excitonic characteristics regarding wavelength positions are almost preserved.

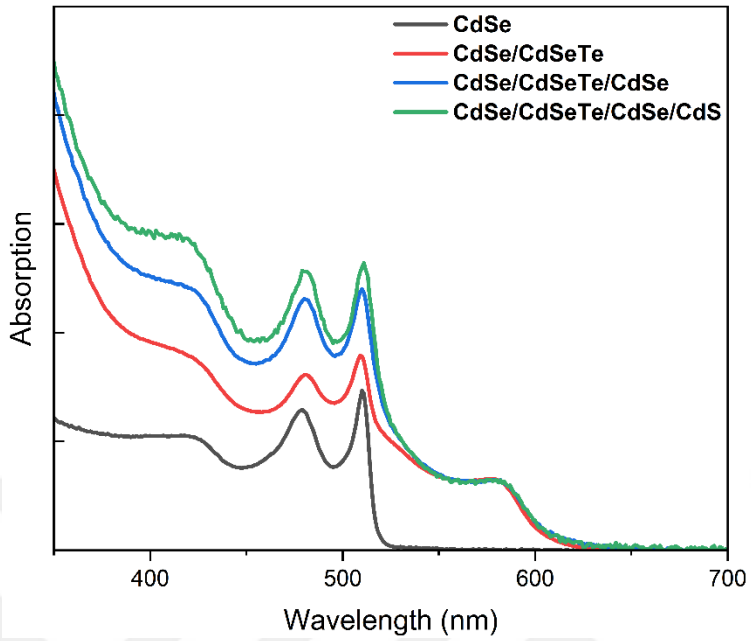

Figure 3.7. Absorption spectra of the CdSe core, CdSe/$CdSe_{0.6}Te_{0.4}$ core/crown, CdSe/$CdSe_{0.6}Te_{0.4}$/CdSe core/multicrown, CdSe/$CdSe_{0.6}Te_{0.4}$/CdSe/CdS core/multicrown NPLs. The absorption spectra of the NPLs having $CdSe_{0.6}Te_{0.4}$ crown is normalized at 550 nm. The spectral wavelengths of the growing peaks indicate the effective growth of each crown layer. The absorption spectra were recorded following the growth of each crown layer.

However, while CdSeTe crown peak emerges around 580 nm, the new growth of CdSe crown layer increases the intensity of the previously formed peak at 510 nm. A new peak in the absorption spectra at ~ 410 nm, corresponding to the excitonic transitions of 4 ML CdS, might be used to confirm the formation of the last CdS crown layer. Due to the lateral thickness of this layer being relatively small, the peak appears barely.

Upon the formation of a pure CdTe crown (for CdSe/$CdSe_{1-x}Te_x$/CdSe/CdS with x=1.00), a new peak arises at ~ 556 nm. The absorption peak at lower energies corresponds to an alloyed type-II crown. The absorption peak of the crown varies with the amount of Te due to the band mixing effect.

Absorption and PL spectra of 4 ML CdSe/$CdSe_{1-x}Te_x$/CdSe/CdS core/multicrown NPLs are presented in Figure 3.8. This graph indicates that the emission of core/multicrown NPLs has been consistently tuned from ~ 582 nm (for $CdSe_{1-x}Te_x$ crown with x=0.05) to ~ 665 nm (for $CdSe_{1-}$

$_xTe_x$ crown with x=1.00) and Stokes shift has been increased continually by enhancing the proportion of Te in the crown layer. While CdSe core-only NPLs exhibit ~ 2 nm Stokes shift, this value spikes up to ~ 107 nm for CdSe/$CdSe_{0.0}Te_{1.0}$/CdSe/CdS core/multicrown NPLs (Figure 3.9.). By tailoring the crown layer's composition, the consistent spectral shift in the emission can be explained by the decrease in hole energy levels. Furthermore, compared to CdSe core-only NPLs, the emission spectra of CdSe/$CdSe_{1-x}Te_x$/CdSe/CdS core/multicrown NPLs are substantially broad. This feature is typical for type-II colloidal semiconductor nanocrystals and can potentially be caused by spatially indirect exciton recombination [54]. Te atoms serve as deep hole-trap sites when $x \leq 0.10$, which results in greater broadened emission when compared to other compositions. The change from quasi type-II electronic structure to the type-II electronic structure can explain this phenomenon [46].

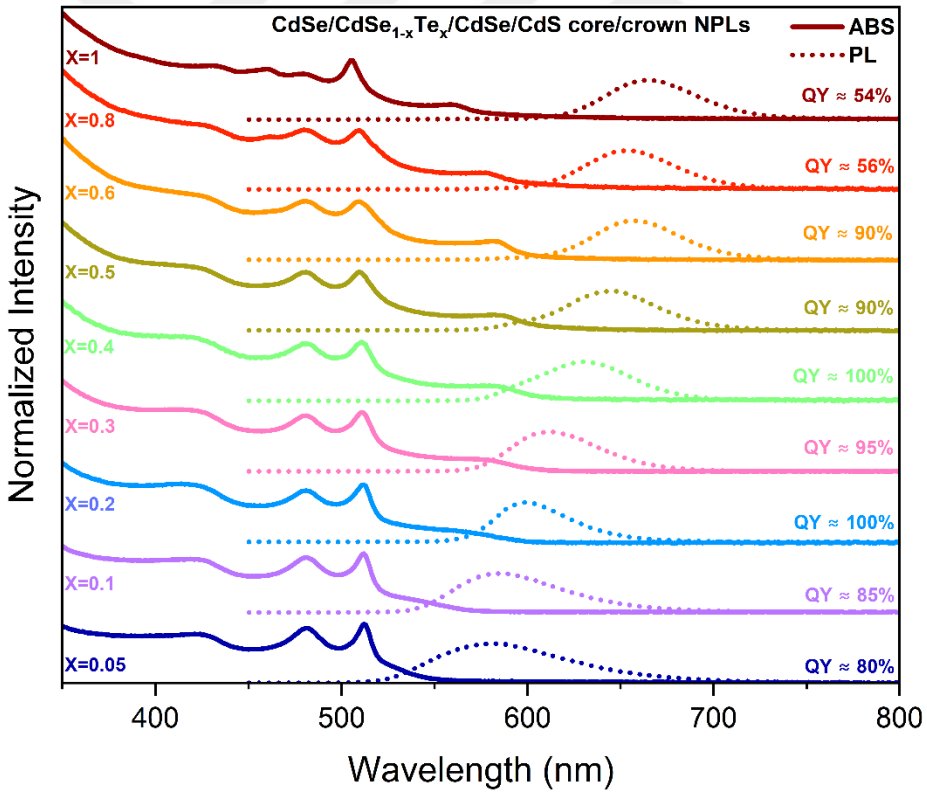

Figure 3.8. Absorption and photoluminescence spectra progression associated with PLQY parameterized with respect to the $CdSe_{1-x}Te_x$ crown composition.

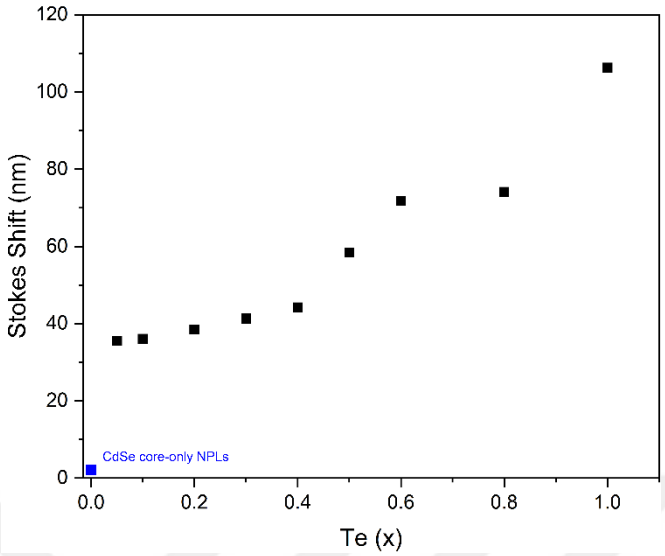

Figure 3.9. Schematic illustrating Stokes shift of CdSe core-only and CdSe/$CdSe_{1-x}Te_x$/CdSe/CdS core/multicrown NPLs.

The improved PLQY is caused by an increase in the possibility of electron and hole wave function overlap when the concentration of Se becomes higher in the crown region, as compared to a pure CdTe crown (x=1.00). The lattice mismatch between the core and crown regions is reduced when Te atoms are exchanged with Se atoms in the crown area. Consequently, there is a reduced probability of defect existence, which serve as trap sites.

3.3.2. Photoluminescence Spectroscopy

As shown in Figure 3.10, the PL spectra demonstrate the redshift behavior with increasing Te composition in $CdSe_{1-x}Te_x$ crown layer. The redshift of PL peak with the increase in Te content in this layer can be attributed to the valance band moving towards the vacuum level as the Te concentration is increased. This results in decreased excitonic energy and emission peak positions at lower energies.

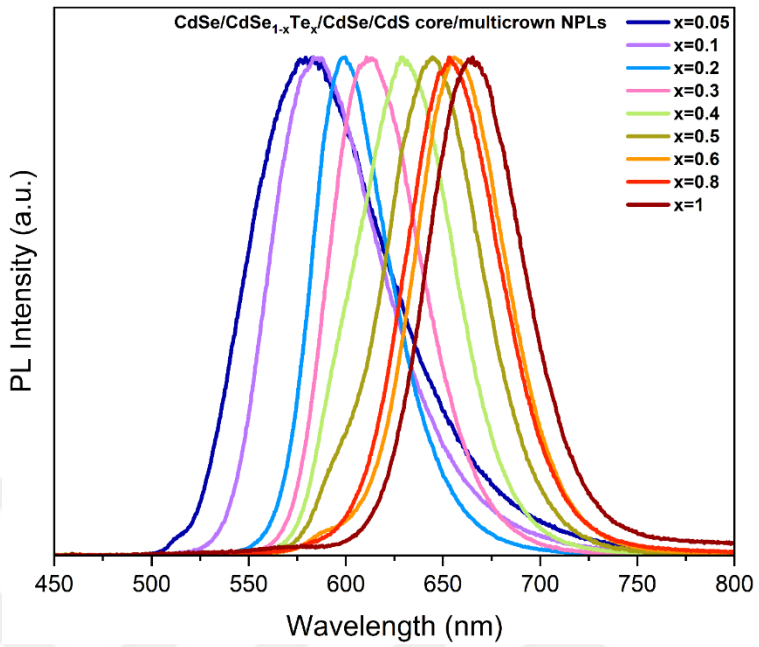

Figure 3.10. PL spectra of the synthesized CdSe/$CdSe_{1-x}Te_x$/CdSe/CdS core/multicrown NPLs.

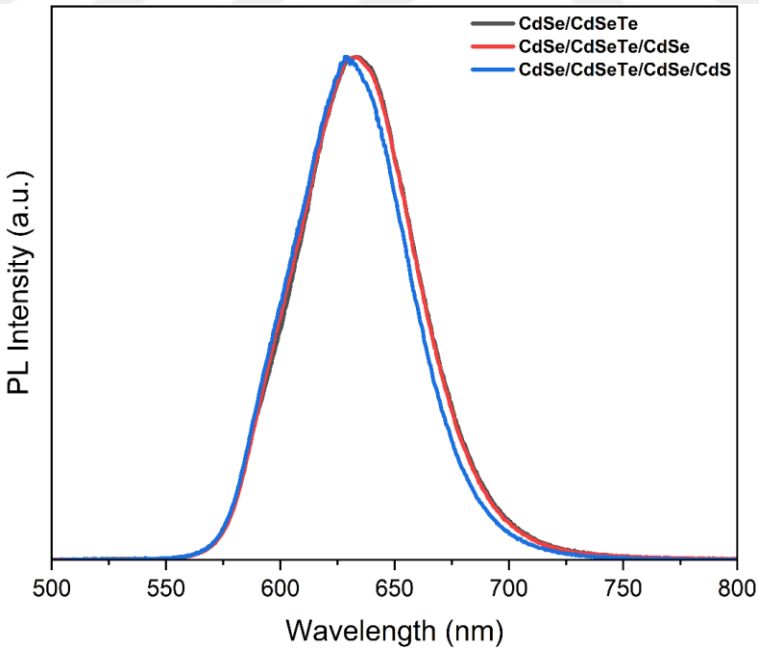

Figure 3.11. PL spectra of the synthesized CdSe/$CdSe_{0.6}Te_{0.4}$ core/crown, CdSe/$CdSe_{0.6}Te_{0.4}$/CdSe core/multicrown, and CdSe/$CdSe_{0.6}Te_{0.4}$/CdSe/CdS core/multicrown NPLs, recorded following growth of each crown layer.

Moreover, the emergence of a broad PL peak at 633 nm with an FWHM of 61 nm signifies the successful growth of the $CdSe_{0.6}Te_{0.4}$ crown layer. In addition, the PL peak does not shift with the following growth of CdSe crown, and FWHM possesses almost the same value, 62 nm. With the growth of the final CdS crown layer, the PL peak blue-shifts from 633 to 631 nm, and FWHM slightly decreases to 60 nm. These slight changes in the PL spectra as the subsequent crown layers grow can be attributed to the built-up strain and the change in the dielectric medium (Figure 3.11.) [55].

3.3.3. Time-Resolved Fluorescence

Studying the kinetics of excited states in fluorescent materials is made possible by practical time-resolved fluorescence spectroscopy. The fundamental idea is to use a short light pulse to excite a sample and then analyze the fluorescence intensity released over time. The way that the fluorescence intensity decays over time sheds light on a number of processes, including quenching, energy transfer, and molecular interactions. Time-resolved fluorescence is explained by the exponential decay of excited states, which is expressed by the following equation:

$$I(t) = I_0 e^{-t/\tau} \tag{3.2}$$

where $I(t)$ is the fluorescence intensity at time t, I_0 is the initial intensity, and τ is the fluorescence lifetime. One of the most important parameters in this method is the fluorescence lifetime, which is the mean duration of time the emitter stays in the excited state before returning the ground state by nonradiative processes or emitting a photon (via radiative decay). Scientists can infer important information on the material's photophysical features by examining the decay profiles.

We used time-resolved fluorescence spectroscopy to better comprehend the excitonic features of $CdSe/CdSe_{1-x}Te_x/CdSe/CdS$ core/multicrown NPLs, depending on the crown layer's composition. To prevents multiexciton generation, TRF measurements were taken using low concentration core/multicrown NPL solutions at low excitation intensities. Fluorescence decay curves of $CdSe/CdSe_{1-x}Te_x/CdSe/CdS$ core/multicrown NPLs with various compositions are presented in Figure 3.12. Previous studies showed that multiexponential PL decay is seen in NPLs due to multi-channel radiative and nonradiative pathways. The decay curves were fitted by using three exponential decay functions. The values of the fittings (lifetimes, coefficient of each lifetime, and intensity averaged lifetimes) are summarized in Table 3.1.

The intensity averaged lifetime of CdSe/$CdSe_{0.0}Te_{1.0}$/CdSe/CdS core/multicrown NPLs is 286.4 ns, which is the highest value between the samples, and comparable to the previously reported PL lifetimes of CdSe/$CdSe_{1-x}Te_x$ core/crown NPLs, nevertheless; one orders of magnitude longer than the PL lifetime of pristine CdSe core NPLs [46]. The presence of type-II band alignment in these NPLs, where holes are located around the crown and electrons confined in the core, is supported by the long PL lifetime seen in comparison to the pristine CdSe NPLs.

Previous studies have shown that CdSe/$CdSe_{1-x}Te_x$ core/crown NPLs exhibit a quasi type-II electronic structure when $x \leq 0.10$ where Te atoms serve as deep hole trap sites and holes localize around these atoms. On the other hand, for $x \geq 0.25$ the NPLs exhibit a type-II electronic structure [46]. As we know from Section 2.3.1, the PL lifetime of type-II electronic structure is longer than the others; thus, we expect longer lifetime for $x \geq 0.25$. Moreover, another study demonstrates that the PL lifetime of CdS/$CdSe_{1-x}Te_x$ core/crown NPLs is shorter than that of CdS/CdTe core/crown NPLs since decreasing Te concentration makes CB offset fall [55]. The primary cause of this lifetime shortening with increasing Se concentration is an increase in the photogenerated carriers' wavefunction overlap, which raises the oscillator strength and encourages radiative recombination. In the light of these, our results seem to correlate well with previous studies.

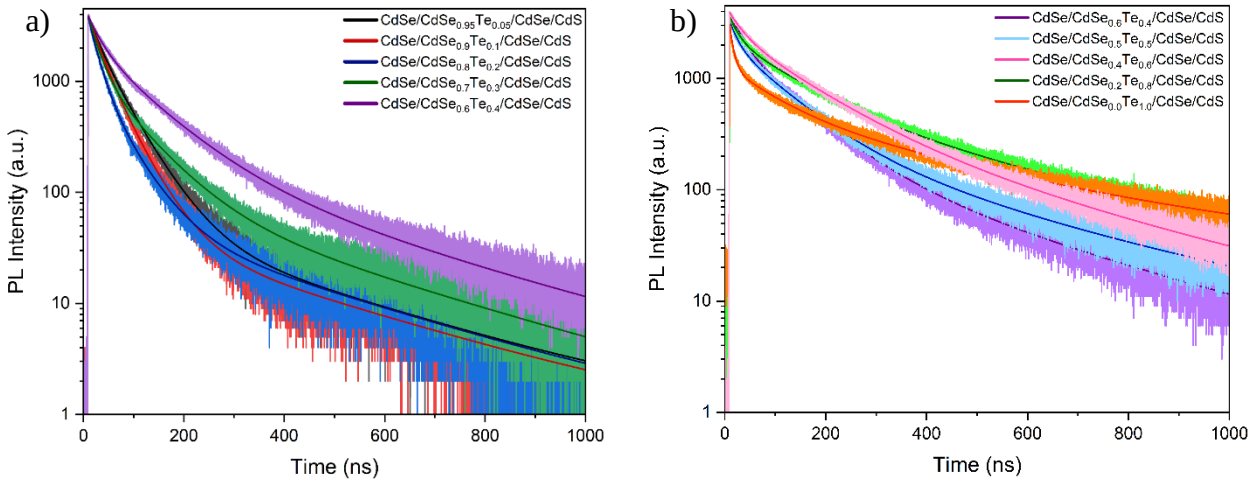

Figure 3.12. TRPL decay curves of CdSe/$CdSe_{1-x}Te_x$/CdSe/CdS core/multicrown NPLs for various compositions.

Table 3.1. Summary of the decay components of the CdSe/$CdSe_{1-x}Te_x$/CdSe/CdS core/multicrown NPLs.

Sample	TRF decay components									Intensity average lifetime $\frac{\sum A_i\tau_i^2}{\sum A_i\tau_i}$ (ns)
	τ_1 (ns)	A_1	τ_2 (ns)	A_2	τ_3 (ns)	A_3	$\frac{A_1\tau_1}{\sum A_i\tau_i}$ (%)	$\frac{A_2\tau_2}{\sum A_i\tau_i}$ (%)	$\frac{A_3\tau_3}{\sum A_i\tau_i}$ (%)	
CdSe/ $CdSe_{0.95}Te_{0.05}$/CdSe/CdS	53.4	2426.9	21.6	1313	298	60.9	73.6	16.1	10.3	73.5
CdSe/ $CdSe_{0.90}Te_{0.10}$/CdSe/CdS	48.1	1861	23.1	1829.7	285.4	45.5	61.8	29.2	9	62.1
CdSe/ $CdSe_{0.80}Te_{0.20}$/CdSe/CdS	53.7	1068.1	18.8	2650.6	298.4	60.9	45.8	39.7	14.5	75.3
CdSe/ $CdSe_{0.70}Te_{0.30}$/CdSe/CdS	75.3	1241.5	20	2506	310.2	109.1	52.7	28.2	19.1	104.5
CdSe/ $CdSe_{0.60}Te_{0.40}$/CdSe/CdS	95.2	1924.9	25.2	1646	315.9	234.2	61.3	13.9	24.8	140.1
CdSe/ $CdSe_{0.50}Te_{0.50}$/CdSe/CdS	94.6	1756.7	15.3	1304	325.1	320.5	57.2	6.9	35.9	171.9
CdSe/ $CdSe_{0.40}Te_{0.60}$/CdSe/CdS	27.7	1314	125.3	2133.1	358.5	436.8	47.4	49.5	3	196.9
CdSe/ $CdSe_{0.20}Te_{0.80}$/CdSe/CdS	379.5	620.8	117.6	1636.5	17.7	1394	52	42.5	5.5	248.4
CdSe/ $CdSe_{0.0}Te_{1.0}$/CdSe/CdS	382.8	474.4	92	752.5	8	1814	68.4	26.1	5.5	286.4

3.3.4. Reabsorption Measurements of CdSe/CdSeTe/CdSe/CdS Nanoplatelets

Reabsorption of luminophores in LSC is one of the critical optical loss parameters together with PLQY. To enhance the optical efficiency of LSC, the luminophores should be designed carefully. In this regard, CdSe/CdSeTe/CdSe/CdS core/multicrown NPLs were engineered for large Stokes shift and PLQY. The overall optical efficiency decreases exponentially with the number of reabsorption events. Therefore, minimizing the reabsorption probability to near zero is essential for achieving large-scale, high-performance LSCs. For the large Stokes shift, there should be negligible or no spectrum overlap between luminophores' absorption and emission spectra [56].

As illustrated in Figure 3.8, increasing the tellurium concentration in the CdSeTe crown layer of our NPLs results in a decreased overlap between the absorption and emission spectra. However, this increase in tellurium concentration also leads to a reduction in PLQY. Given that both parameters significantly impact the optical efficiency, further investigation through reabsorption measurements of CdSe/CdSeTe/CdSe/CdS nanoplatelets is also conducted.

As seen in Figure 3.13, a one-dimensional liquid waveguide with an excitation source mounted on a portable stage was used to assess the reabsorption losses in the NPLs. Through the use of a multimode optical fiber and lens system, the portable excitation source adjusts the optical path distance to the fixed emission detection spectrometer. Reabsorption losses are analyzed by measuring the PL spectra with changing optical path distance, L, up to 90 cm, keeping the excitation source power constant during measurement. To make a reliable comparison among synthesized NPLs, the optical densities of solutions were kept constant (OD=3) over t=1 mm (which is the thickness of the quartz cuvette) at their e-hh absorption peaks.

Although CdSe/$CdSe_{0.2}Te_{0.8}$/CdSe/CdS and CdSe/$CdSe_{0.0}Te_{1.0}$/CdSe/CdS core/multicrown NPLs were successfully synthesized, their PLQY decreases sharply since NPLs with high concentration of tellurium react with the oxygen of ambient air. Considering the long-term performance and stability of the LSCs, reabsorption measurements were not performed on these NPLs and they were not used as luminophores in LSC fabrication.

The hollow fused silica waveguide was meticulously filled with the solutions to prevent the formation of air bubbles in the optical path, which can lead to additional scatterings and bias. By moving the excitation source to systematically altered values of L, which is the optical path

distance between the excitation source and the waveguide's collecting end, the PL emission spectra were measured. The dashed lines in Figure 3.14. show the half PL intensity of different compositions of CdSe/CdSeTe/CdSe/CdS core/multicrown NPLs. Our half-length ($L_{1/2}$) for all measured compositions of CdSe/CdSeTe/CdSe/CdS core/multicrown NPLs surpassed the previously reported Cu^+ doped CdSe QDs [38], exceeding ~10 cm.

As the length L increases, all luminophores exhibit a decrease in PL intensity along with a red shift in their spectra. This reduction in PL emission intensity, coupled with the red shift in the PL emission spectra can be attributed to reabsorption losses occurring at the higher energy side of the PL emission spectrum. To be compared fairly of different luminophores, the red shift is calculated as

$$\Delta\lambda = \lambda_{max}(d_{max}) - \lambda_{max}(d_{min}) \tag{3.3}$$

where $\lambda_{\max}(\mathrm{d})$ means the wavelength at which the emission attains its maximum, and d is the length of the optical path at which the spectrum was recorded. Our synthesized CdSe/$CdSe_{1-x}Te_x$/CdSe/CdS core/multicrown NPLs show a minimum red shift of ~5 nm (for x=0.4), and a maximum red shift of ~11 nm (for x=0.05) for the optical path length of 90 cm. These NPLs perform better compared with the CdSe QDs showing ~12 nm red shift for the optical path length of 2.5 cm [35], and 4 ML Cu^+ doped CdSe NPLs showing ~40 nm red shift for the optical path length of 80 cm [38].

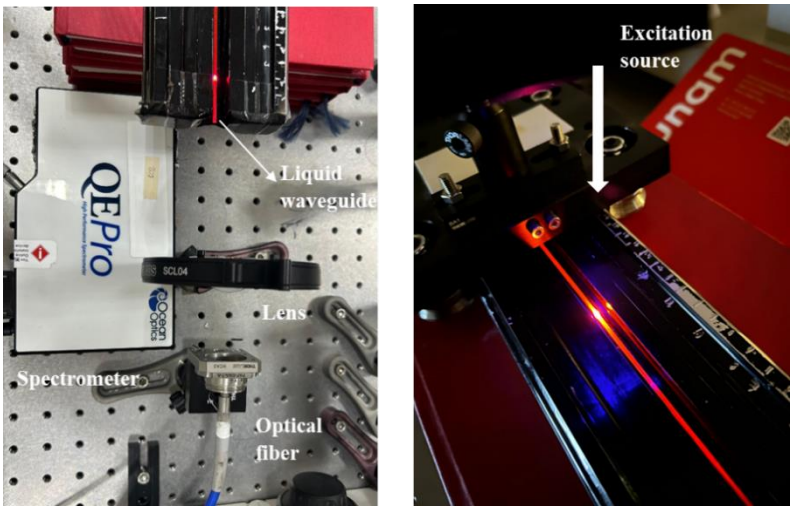

Figure 3.13. Photographs for our reabsorption measurement setup of CdSe/CdSeTe/CdSe/CdS core/multicrown NPLs.

a)

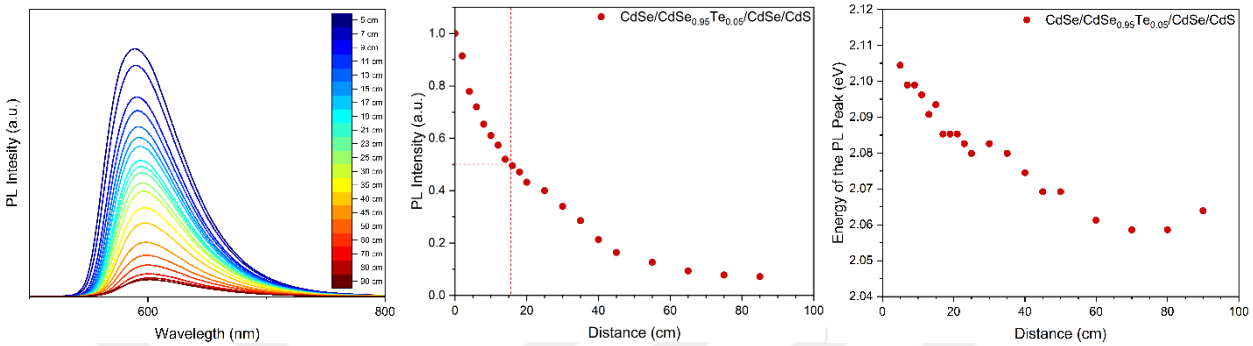
PL Intesity (a.u.)
Wavelegth (nm)
PL Intensity (a.u.)
Distance (cm)
CdSe/CdSe0.95Te0.05/CdSe/CdS
Energy of the PL Peak (eV)
Distance (cm)
CdSe/CdSe0.95Te0.05/CdSe/CdS

b)

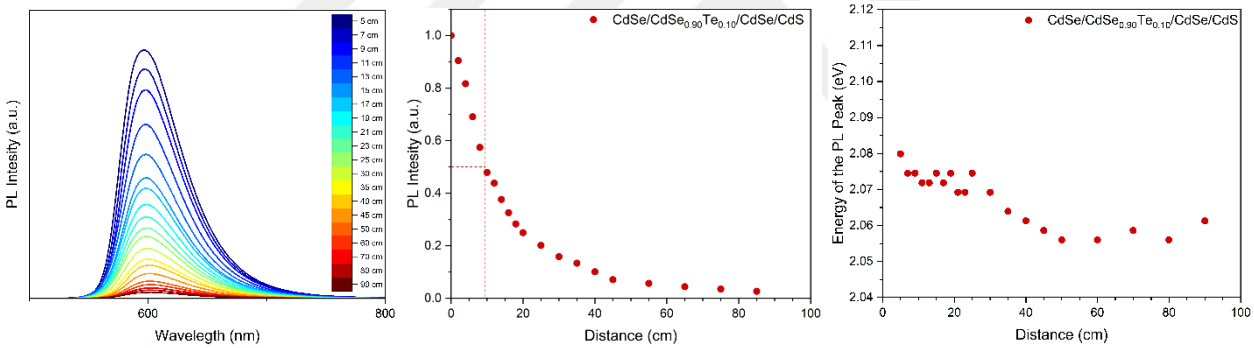
PL Intesity (a.u.)
Wavelegth (nm)
PL Intesity (a.u.)
Distance (cm)
CdSe/CdSe0.90Te0.10/CdSe/CdS
Energy of the PL Peak (eV)
Distance (cm)
CdSe/CdSe0.90Te0.10/CdSe/CdS

c)

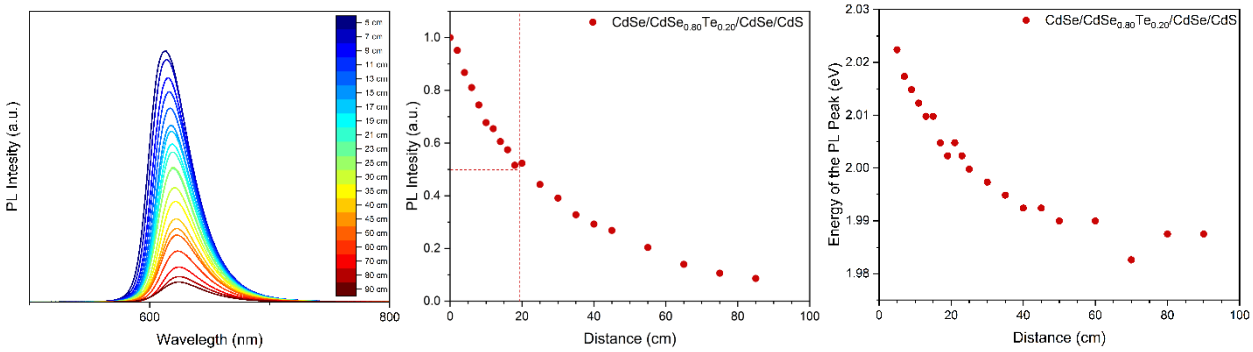
PL Intesity (a.u.)
Wavelegth (nm)
PL Intesity (a.u.)
Distance (cm)
CdSe/CdSe0.80Te0.20/CdSe/CdS
Energy of the PL Peak (eV)
Distance (cm)
CdSe/CdSe0.80Te0.20/CdSe/CdS

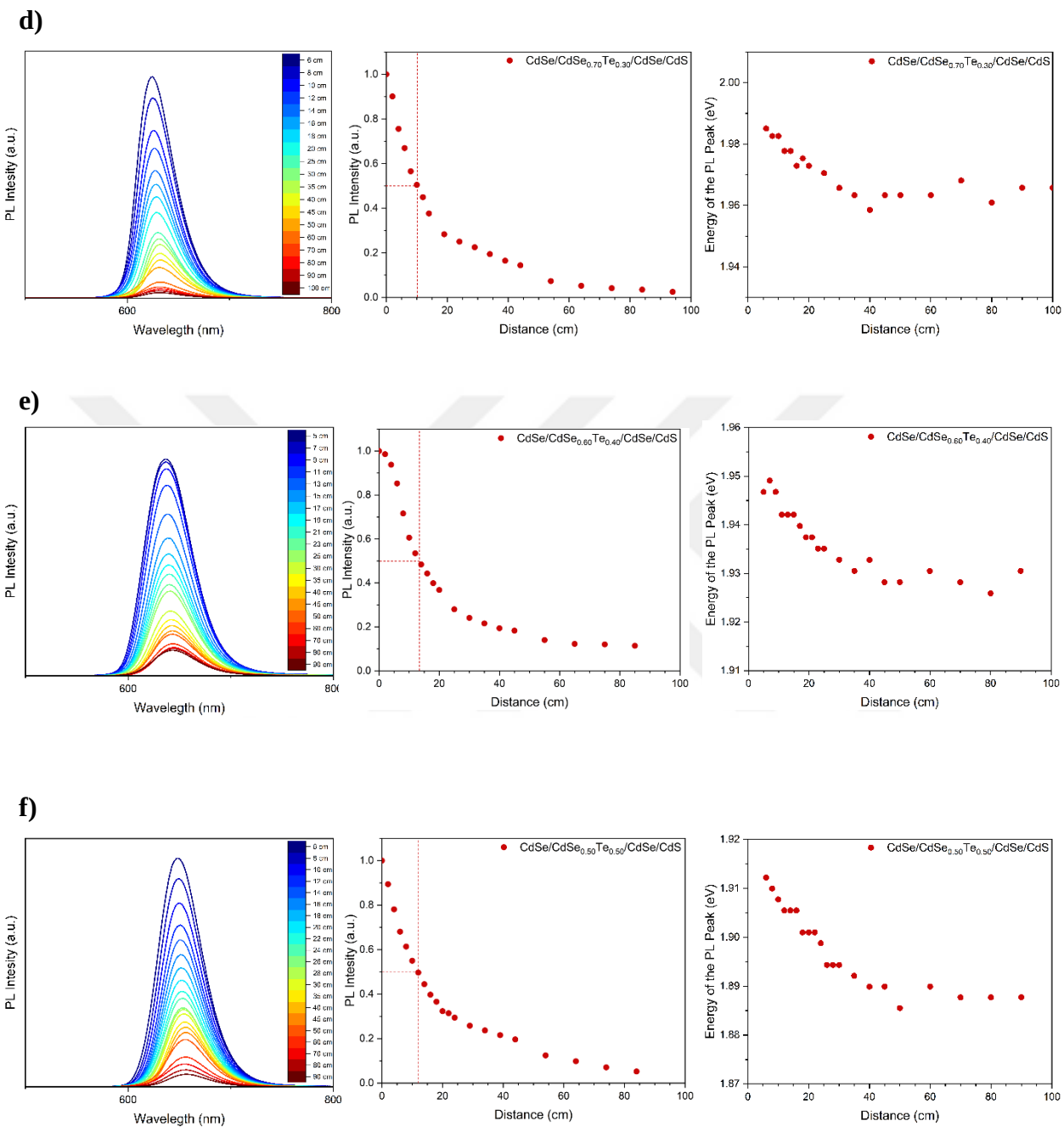

Figure 3.14. PL emission spectra as a function of the wavelength and excitation distance, and photon energy of the PL peak as a function of the excitation distance for a) CdSe/CdSe$_{0.95}$Te$_{0.05}$/CdSe/CdS core/multicrown NPLs, b) CdSe/CdSe$_{0.90}$Te$_{0.10}$/CdSe/CdS core/multicrown NPLs, c) CdSe/CdSe$_{0.80}$Te$_{0.20}$/CdSe/CdS core/multicrown NPLs, d) CdSe/CdSe$_{0.70}$Te$_{0.30}$/CdSe/CdS core/multicrown NPLs, e) CdSe/CdSe$_{0.60}$Te$_{0.40}$/CdSe/CdS core/multicrown NPLs, and f) CdSe/CdSe$_{0.50}$Te$_{0.50}$/CdSe/CdS core/multicrown NPLs.

As demonstrated in Figure 3.9, an increase in the Te composition of the $CdSe_{1-x}Te_x$ crown layer results in a significant Stokes shift, thereby reducing the probability of reabsorption. However, the same figure also indicates that a higher Te portion leads to a decrease in PL-QY. Consequently, slight fluctuations in the half PL intensity are observed due to the interplay between the varying Stokes shift and PL-QY (Figure 3.15.).

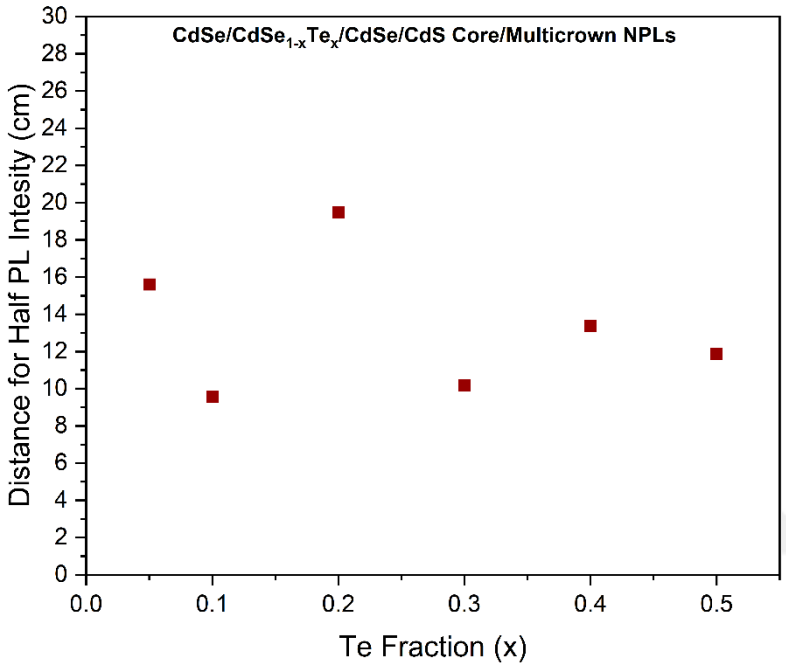

Figure 3.15. Graph showing the half PL intensity distance as a function of Te (x) fraction in the composition of $CdSe/CdSe_{1-x}Te_x/CdSe/CdS$ core/multicrown NPLs.

Chapter 4

Luminescent Solar Concentrators of CdSe/CdSeTe/CdSe/CdS Core/Multicrown Type-II Nanoplatelets

Luminescent solar concentrators (LSCs) absorb incident sunlight normal to their surface and emit light as a result of sunlight absorption to be collected and directed laterally to their periphery via their slab waveguide structure. LSCs increase the efficiency of photovoltaic systems. Various materials are used in LSCs as a luminophore such as organic dyes, rare earth ions and colloidal semiconductors. Among these materials, CdSe/CdSeTe/CdSe/CdS core/multicrown type-II NPLs outstand with their excellent optical features. Since type-II band alignment separates electron and hole pairs spatially, the probability of nonradiative recombination reduces, and photoluminescence efficiency over long distances of propagation improves. As mentioned in Chapter 3, with changing the composition of $CdSe_{1-x}Te_x$ crown layer, absorption and PL emission spectra can be conveniently tuned. Thus, our luminophores show almost no absorption and emission spectral overlap. Moreover, possible aggregation of NPLs may cause additional scattering centers and reduce the optical performance of LSCs, particularly in large-scale devices. However, our CdSe/CdSeTe/CdSe/CdS core/multicrown NPLs are stable in long term owing to CdS crown layer, making them excellent candidate for the fabrication of LSCs.

In this chapter, fabrication of LSC will be explained and demonstrated using our $CdSe/CdSe_{1-x}Te_x/CdSe/CdS$ core/multicrown NPLs for several compositions ($0.3 \leq x \leq 0.6$), and their characterization results will be analyzed, and compared with previously reported efficiency values.

4.1. Operating Principle of Luminescent Solar Concentrators

The theory behind a luminescent solar concentrator is to harvest sunlight via the surfaces of the optical medium that are embedded with luminophores. The optical medium can be a transparent or translucent plastic or glass plate. A portion of the incoming light is reflected upon interaction with the optical medium, and another portion is transmitted through the LSC. The remaining light within the slab is then absorbed by luminophores, which emit light at a longer wavelength and with a particular PLQY.

Subsequently, luminescence is transferred to the LSC's edges via total internal reflection and connected to a solar cell. While a significant amount sheers the front and back surfaces since it is not trapped, overlap of the emission and absorption bands causes reabsorption losses. Even though of all of these losses, LSC raises solar energy conversion efficiency and offers affordable solar energy harvesting technology (Figure 4.1.) [57].

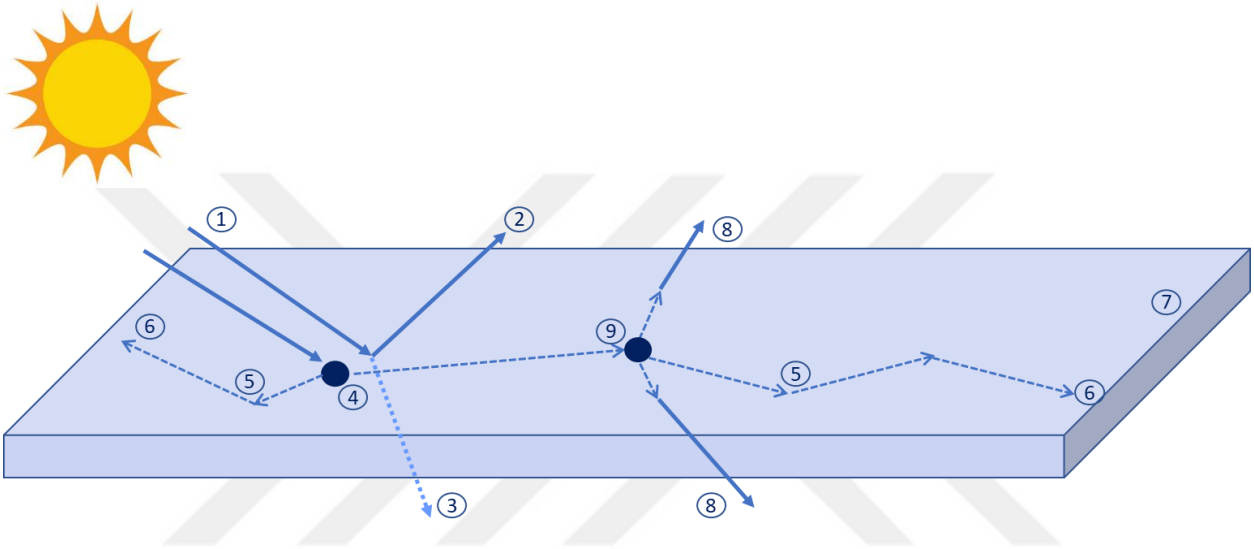

Figure 4.1. Operating principle of LSCs [57].

4.2. Fabrication of Luminescent Solar Concentrators

Chemicals

Poly(lauryl methacrylate), diphenyl(2,4,6-trimethylbenzoyl)phosphine oxide, ethylene glycol dimethacrylate and ethanol were purchased from Sigma Aldrich.

After the completing of CdSe/CdSeTe/CdSe/CdS core/multicrown NPLs synthesis, the 10% of the solution was put into a new falcon and precipitated by adding ethanol in 1:1 ratio with the solution. Following the precipitation step, the optical density of the 10% solution was calculated from the UV-visible spectrum. According to this calculation, optical density of the remaining precipitate (90% of the solution) was determined.

Poly(lauryl methacrylate) was chosen to be used as a polymer host material to make high-quality NPL-polymer nanocomposite because its long side chains prevent the clustering of NPLs and it has low optical absorption in the visible band. Regardless of their precipitated amount, NPLs may be dispersed in 2 mL poly(lauryl methacrylate) with the help of a vortex machine. Since PL-QY of CdSe/CdSeTe/CdSe/CdS core/multicrown NPLs are affected by oxygen, mixing was carried out inside a N_2-filled glove box. The mixture was left to stir for almost 4 h until it was uniformly dispersed (Figure 4.2a).

The host matrix was prepared by mixing 0.25 wt% diphenyl(2,4,6-trimethylbenzoyl)phosphine oxide, 20 wt% ethylene glycol dimethacrylate as a crosslinker, and 80 wt% lauryl methacrylate in the dark environment because diphenyl(2,4,6-trimethylbenzoyl)phosphine oxide, the photo initiator, is sensitive to light (Figure 4.2b). First, the outer surface of the falcon tube was wrapped and then the mixture was put into it. The mixture was stirred with a magnetic stirring bar in the dark environment for 4 h. These chemicals are chosen as the host matrix because their mixture has an appropriate refractive index and high transparency, and disperse our NPLs well.

Next step was mixing with a magnetic stirring bar the 23-optical density CdSe/$CdSe_{1-x}Te_x$/CdSe/CdS (for $0.3 \leq x \leq 0.6$) core/multicrown NPLs in 2 mL lauryl methacrylate with 34.5 mL of pre-prepared host matrix solution in a falcon tube wrapped with aluminum foil in the dark glove box. The mixing takes at least 6 h to obtain a homogenous luminophore solution (Figure 4.2c).

The glass layers offer a low-autofluorescence, low-roughness, low-loss cladding that has minimal permeability to oxygen and water. Moreover, their reflection losses are 7-11%. Since there is a small difference in terms of the optical efficiency compared to other usable materials like quartz plates and various types of polymers, cost-related issues and secondary properties such as shelf lifetime are taken into consideration for choosing glass as the substrate.

In the light of these discussions, two square borofloat glasses with a lateral length of 5 cm were attached one on top of the other with a transparent acrylic tape from their corners. The luminophore solution was filled slowly avoiding bubbles, which otherwise drops the optical efficiency, with hypodermic needle from the gap between the glasses until the all lateral area was covered. After filling the LSC devices, they were immediately photopolymerized under uniform 365 nm UV exposure for 20, 25 and 30 min (Figure 4.2d-e). The material that overspilled the glass surface was

cleaned with the help of isopropanol since it does not dissolve the used polymer host matrix. After this step, the LSC devices were finally ready for measurements.

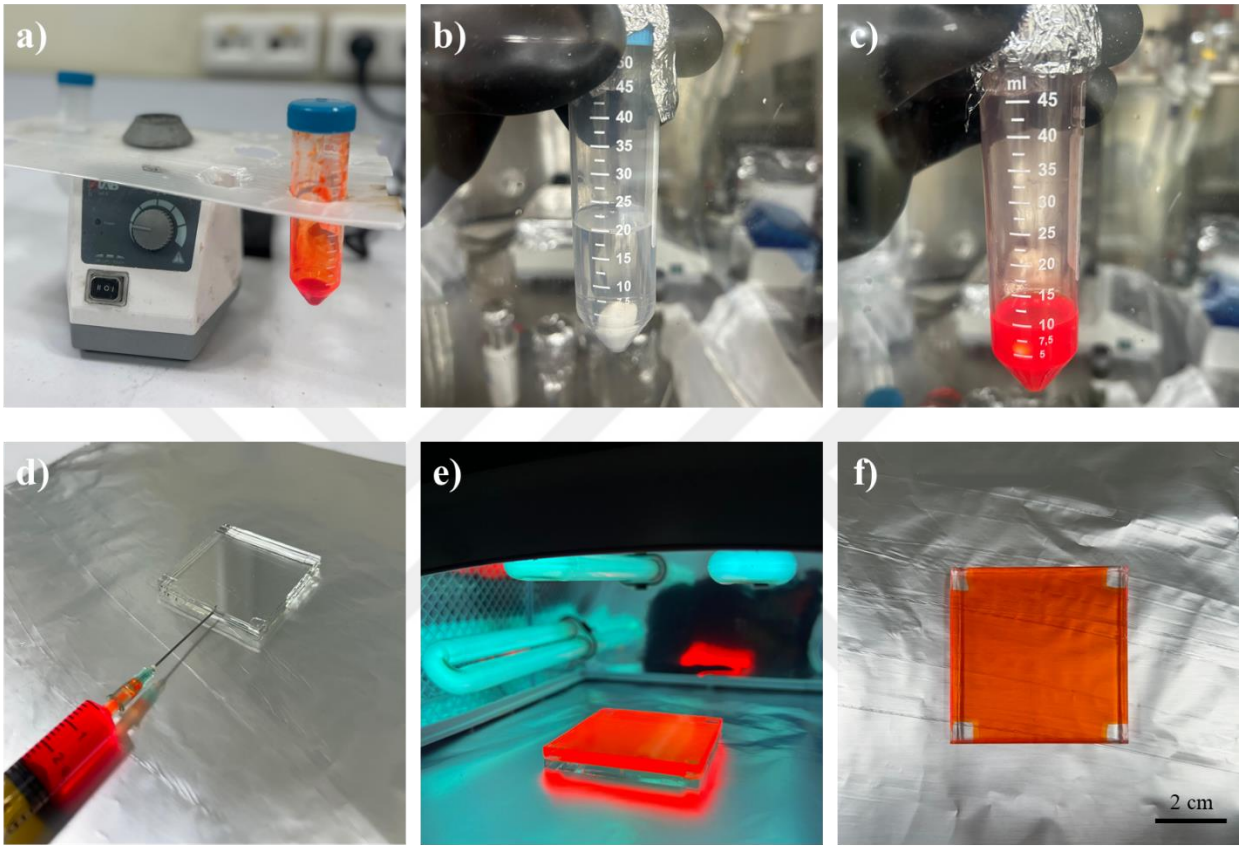

Figure 4.2. Photographs for fabrication steps of a LSC: a) Stirring of NPL-poly(lauryl methacrylate) via a vortex machine and obtaining the mixed b) host matrix, c) mixing NPL-polymer nanocomposite solution, d) filling the glass cell with the NPL-polymer nanocomposite solution with a hypodermic needle, and e) photopolymerization of the NPL-polymer nanocomposite solution in the glass cell using a UV source. f) Photograph of the final fabricated LSC device after the polymerization step.

4.3. Luminescent Solar Concentrator Characterization Setup

After the preparation of LSC prototypes with CdSe/$CdSe_{1-x}Te_x$/CdSe/CdS ($0.3 \leq x \leq 0.6$) luminophores in the polymer matrix for 20, 25 and 30 min photopolymerization time, their power conversion efficiencies (η_{power}) were characterized at the end of several calibration steps.

First of all, irradiance (power density) analyses were performed laterally and vertically depending on the distance between the solar simulator and the optical fiber. The analyses revealed that an increase in the distance between the solar simulator and the fiber results in a decrease in irradiance. Conversely, a decrease in this distance leads to loss of uniformity in the light distribution. According to results, ideal position for LSCs was designated.

Secondly, since our LSC prototypes were 5 χ 5 cm^2 in size, the irradiance measurements were taken from twenty-five points for every 1 cm laterally and vertically. Thus, the total power density at the ideal position was obtained (Figure 4.3). Due to the fact that the measured area was known, it was possible to calculate the total power from the measured power densities.

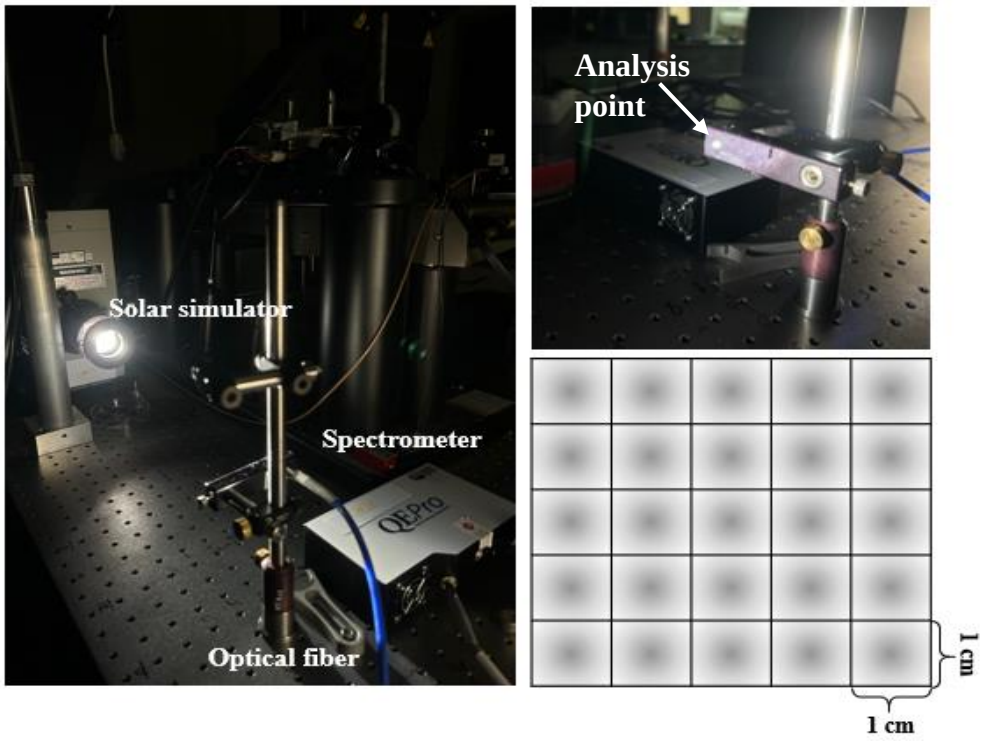

Figure 4.3. Photographs and illustration of the irradiance measurements.

In the next step, the integrated sphere was placed in the same location laterally and vertically using the aforementioned optical fiber. The total power inside the circle of integrated sphere was calculated with the aid of previous power density measurements. Knowing the total power within this circle, correlation with the power density generated in the integrated sphere was established (Figure 4.4).

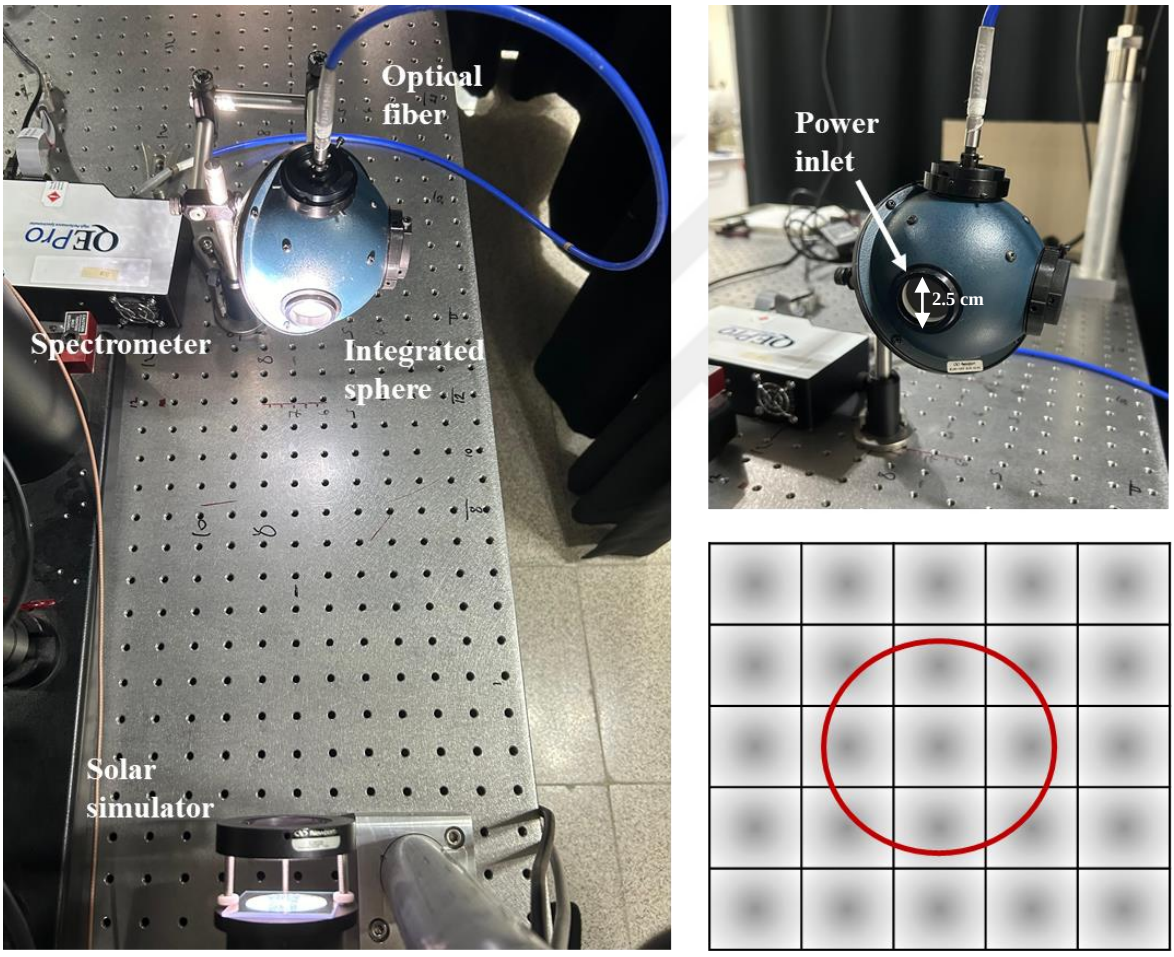

Figure 4.4. Photographs and illustration of the measurement of the power density inside the integrated sphere.

In the final step, the power density generated inside the integrated sphere was measured while LSC prototype was placed in the abovementioned circle of the integrated sphere. In the previous step, the ratio between the local power density and the total power was found. From this ratio, the power can be obtained from the power density generated while the LSC was leaned to the integrated sphere. To prevent any reflection from inside or outside the waveguide, the three edges of LSCs were covered with a black tape except for the edge from which the measurement was taken as shown in Figure 4.5. It is worth mentioning that, given that three edges were covered with a black tape and the measurement aperture of the integrating sphere encompassed half of the LSC's edge, the measured power was multiplied by a factor of eight.

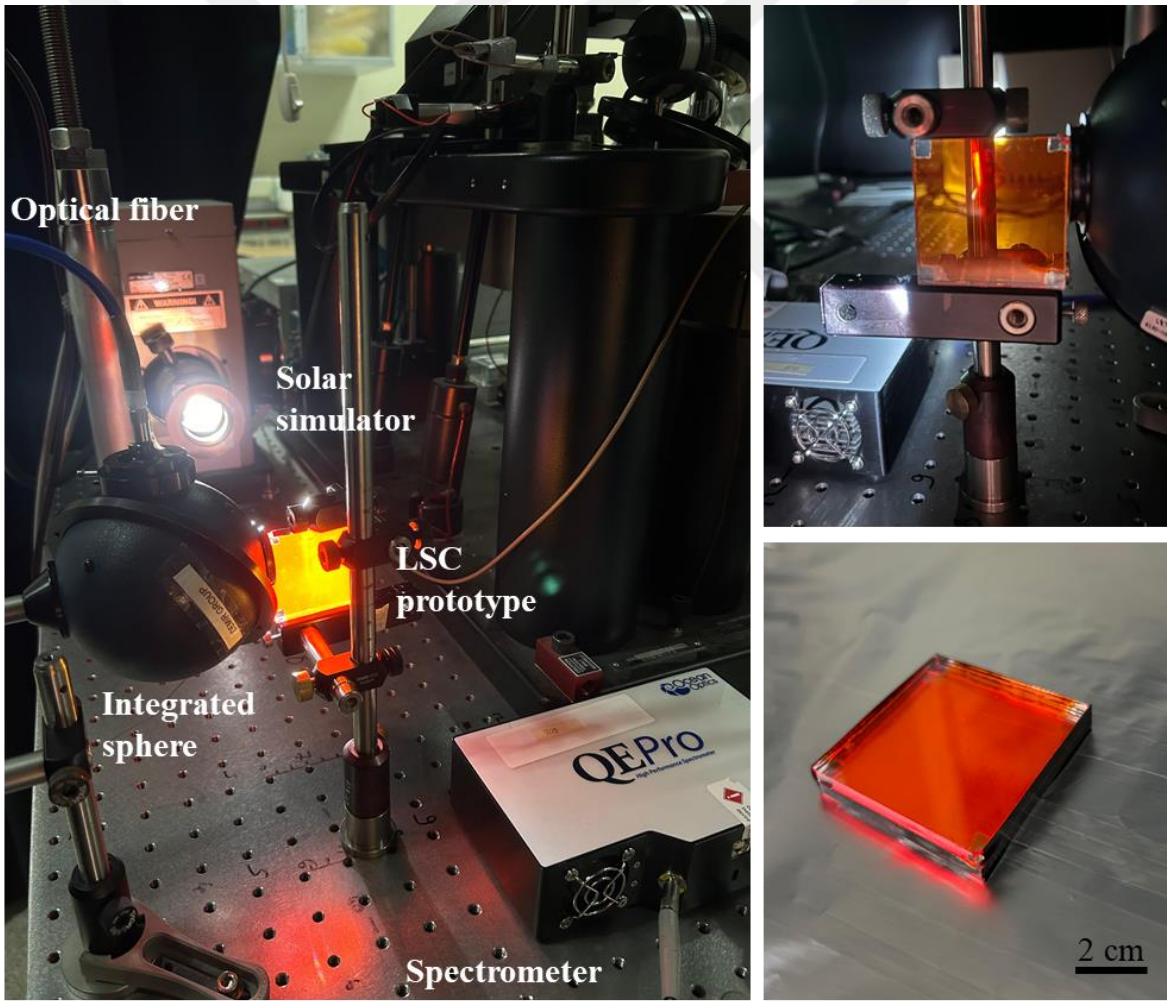

Figure 4.5. Photographs of the power measurement of LSCs leaned to the integrated sphere and of the LSC prototype covered with black tape around three edges (bottom right corner).

4.4. Characterization of Luminescent Solar Concentrators

To understand the performance and possible uses of LSCs in several sectors such as agriculture (as greenhouse panels), construction (as facades of buildings), aerospace (as solar panels on satellites and spacecrafts), characterization results should be evaluated. This section presents an in-depth analysis of LSCs with a spotlight on their optical and photophysical characteristics. The objective of our research here is to provide further insight into the effectiveness and efficiency of the emission and light harvesting processes in this system through the use of several characterization methods, including power and absorbance measurements. Specifically, the impact of extrinsic and structural characteristics, like nanoplatelet composition and photopolymerization duration, on the overall performance of the LSCs is examined. The results of the characterization offer beneficial information that helps us to comprehend the underlying mechanisms influencing the performance of LSCs and guide future design improvements aimed at achieving higher solar energy conversion efficiency.

Several kinds of solar simulators are available that have been developed to resemble the sun's irradiance spectrum (AM 1.5G) as accurately as possible. Some examples of solar simulators are the metal halide lamp, which has a long operational life and a good spectral match to sunlight; the xenon arc lamp, which produces a broad spectrum of light that closely matches the solar spectrum and has high intensity; and the LED-based light source, which is tunable and stable and replicates the solar spectrum while generating less heat and having a long lifespan. In this study, Newport 67005 arc lamp was used and compared with the AM 1.5G solar spectrum.

The standard spectrum at the Earth's surface is known as AM 1.5G, where 'G' stands for global. AM 1.5G is based on a solar energy-related ASTM (American Society of Testing Materials) standard with a specified standard irradiance of 1000 W/m^2. For standard testing of solar energy conversion systems, AM 1.5G is chosen as the reference spectrum. This facilitates to compare measurements of solar conversion efficiency taken at different times and locations.

First of all, the spectral irradiance of our solar simulator was controlled with the datasheet of the company from which we purchased the solar simulator, and it was verified to be matched. (Figure 4.6 and Figure 4.7). The irradiance spectrum of the solar simulator used in this thesis was compared with the standard AM 1.5G (Figure 4.7). The spectrum of the employed solar simulator was

normalized with respect to AM 1.5G. It was determined that the spectral area under the curves between 320-600 nm was exactly equal.

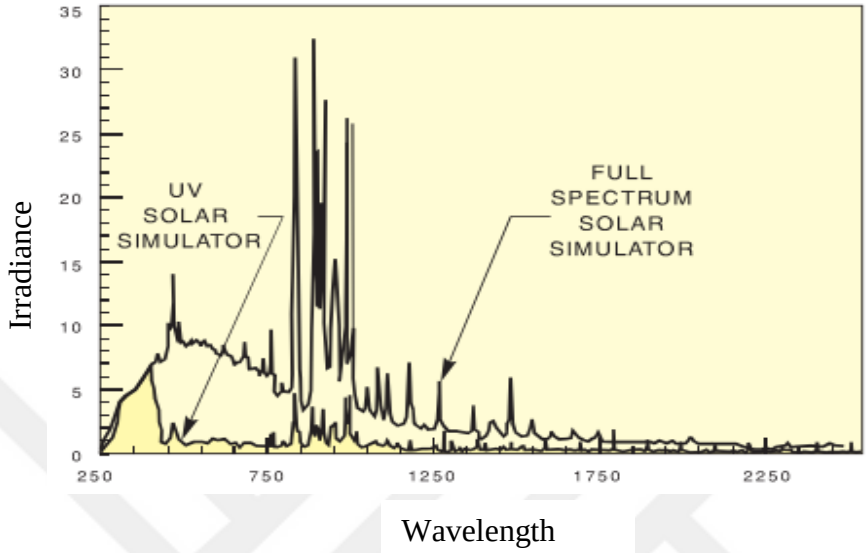

Figure 4.6. Schematic showing the expected irradiance spectra of the purchased solar simulator.

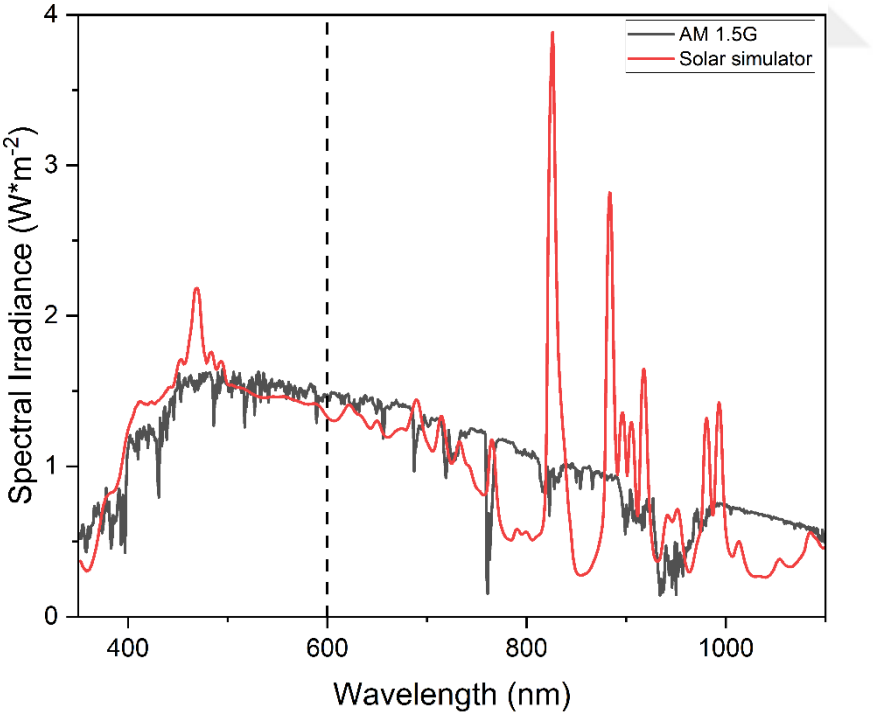

Figure 4.7. Spectral comparison between AM 1.5G and the employed solar simulator. The dashed line indicates that the area under the curves of AM 1.5G and our solar simulator is exactly equal between 320-600 nm.

a)

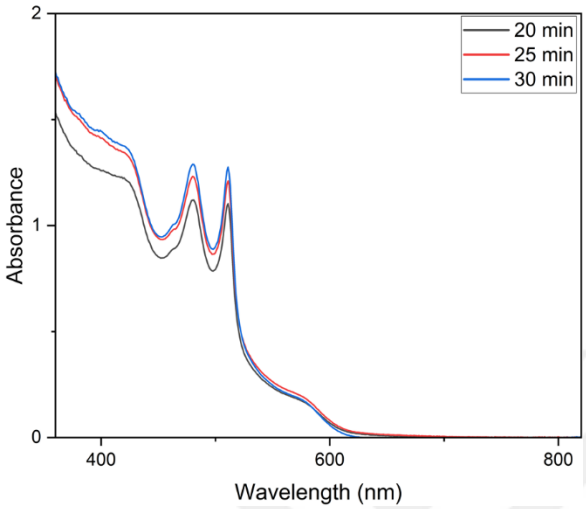
Absorbance
Wavelength (nm)
20 min
25 min
30 min

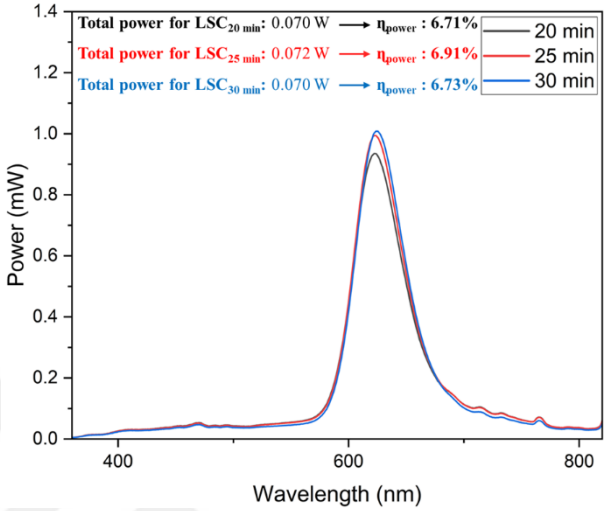
Total power for LSC20 min: 0.070 W → ηpower : 6.71%
Total power for LSC25 min: 0.072 W → ηpower : 6.91%
Total power for LSC30 min: 0.070 W → ηpower : 6.73%
Power (mW)
Wavelength (nm)
20 min
25 min
30 min

b)

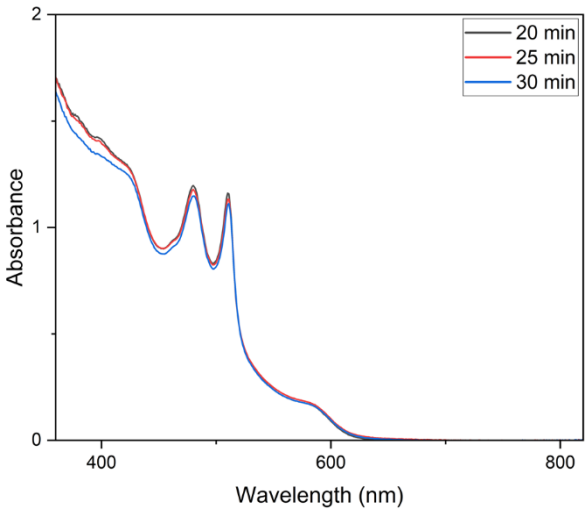
Absorbance
Wavelength (nm)
20 min
25 min
30 min

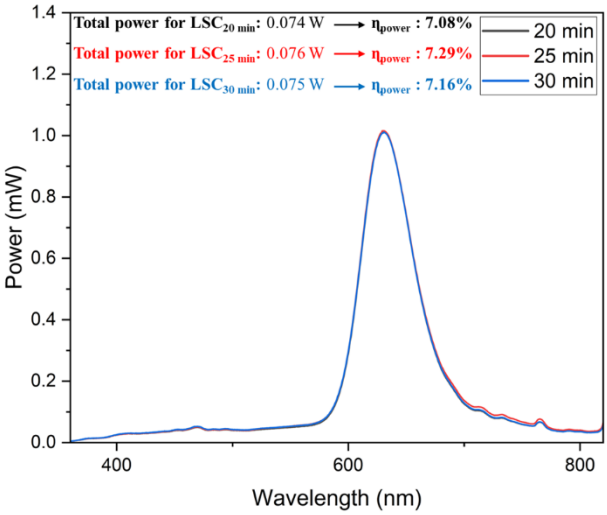
Total power for LSC20 min: 0.074 W → ηpower : 7.08%
Total power for LSC25 min: 0.076 W → ηpower : 7.29%
Total power for LSC30 min: 0.075 W → ηpower : 7.16%
Power (mW)
Wavelength (nm)
20 min
25 min
30 min

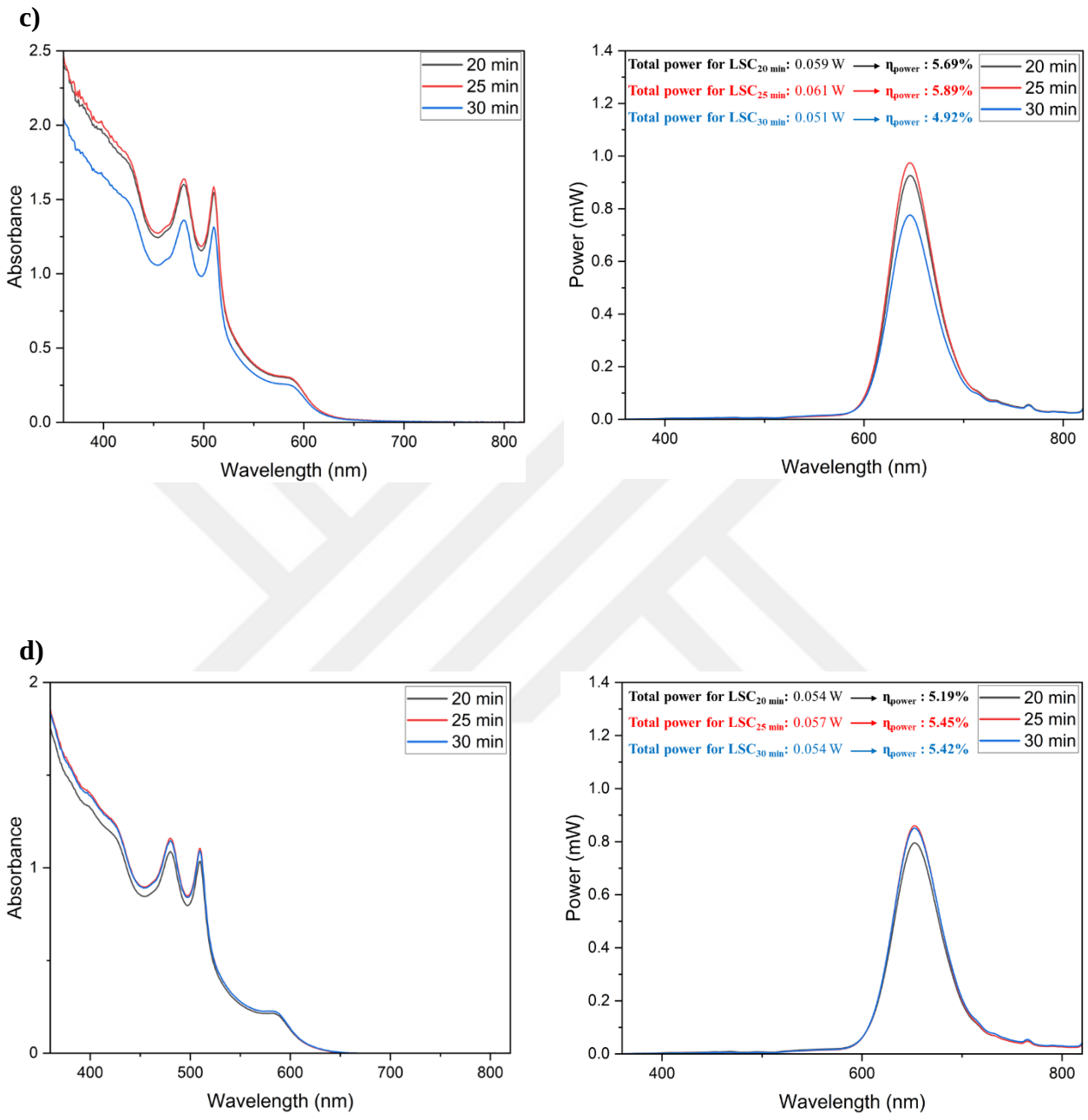

Figure 4.8. Absorbance spectra (left panels) and power measurements (right panels) of LSCs obtained by photopolymerization for 20 min (black), 25 min (red), and 30 min (blue), using a) CdSe/CdSe$_{0.7}$Te$_{0.3}$/CdSe/CdS, b) CdSe/CdSe$_{0.7}$Te$_{0.4}$/CdSe/CdS, c) CdSe/CdSe$_{0.7}$Te$_{0.5}$/CdSe/CdS, and d) CdSe/CdSe$_{0.7}$Te$_{0.6}$/CdSe/CdS NPLs as luminophore.

According to the characterization results presented above, Figure 4.8b shows that, although the LSC photopolymerized for 20 min exhibits higher absorbance, its power conversion efficiency is lower compared to those with longer photopolymerization times. This can be attributed to several factors related to the formation and quality of the polymer matrix in which the luminophores are embedded. These factors are: (i) Incomplete cross-linking or curing of the polymer matrix lead to a less robust and less homogeneous structure. As a result, the matrix can form defects or voids that scatter or absorb light, decreasing the LSC's performance. (ii) The optical clarity and transparency of the polymer matrix causes increased scattering or absorption of light within the LSC. This lowers the overall efficiency by causing the light to be less effectively guided and trapped. (iii) The LSCs' lifetime and potential to maintain optimum light-guiding conditions over time can potentially be impacted by instability. (iv) The efficiency of energy transfer between the polymer matrix and the luminophores hindered by incomplete polymerization results in less effective excitation of the luminophores and reduced re-emission of light at the desired wavelength. These abovementioned mechanisms lower the LSC's performance. Considering all these factors, 25 min photopolymerization offers the highest performance for LSCs including different Te composition in NPLs.

As mentioned in Section 2.4.1, QY of the luminophores used in LSCs is a crucial factor influencing their performance. QY refers to the efficiency at which luminophores convert absorbed photons into emitted photons. QY is related to the photon reabsorption and reemission levels and nonradiative losses and affects light guiding efficiency and power output of the device. Figure 4.9. depicts the highest-performance LSCs with changing Te concentration. Although the absorbance profile over the same range is quite similar for CdSe/$CdSe_{1-x}Te_x$/CdSe/CdS (for $0.3 \leq x \leq 0.5$) NPL embedded LSCs, the LSCs with the luminophores of CdSe/$CdSe_{0.6}Te_{0.4}$/CdSe/CdS possessing the highest QY outperform other devices.

As listed in Table 4.1, our power conversion efficiencies are proportional with QY. The LSC devices including CdSe/$CdSe_{0.6}Te_{0.4}$/CdSe/CdS NPLs having near-unity quantum yield exhibit the highest η_{power}, 7.29%. It is important to highlight that high quantum yield means that a greater portion of absorbed photons are re-emitted as the photoluminescence, enhancing the portion of light that is redirected within the LSC towards the solar cells at the edges. This enhances the power output of the LSC. In addition to that, a high quantum yield reduces the reabsorption losses, where

emitted photons are reabsorbed by other luminophores within the LSC. Reduced reabsorption helps to preserve light intensity as it is guided towards the solar cells. Consequently, quantum yield optimizes the photoluminescence efficiency of the luminophores, minimizing energy losses, enhancing light guiding, and ultimately improving the overall performance and power conversion efficiency of LSCs.

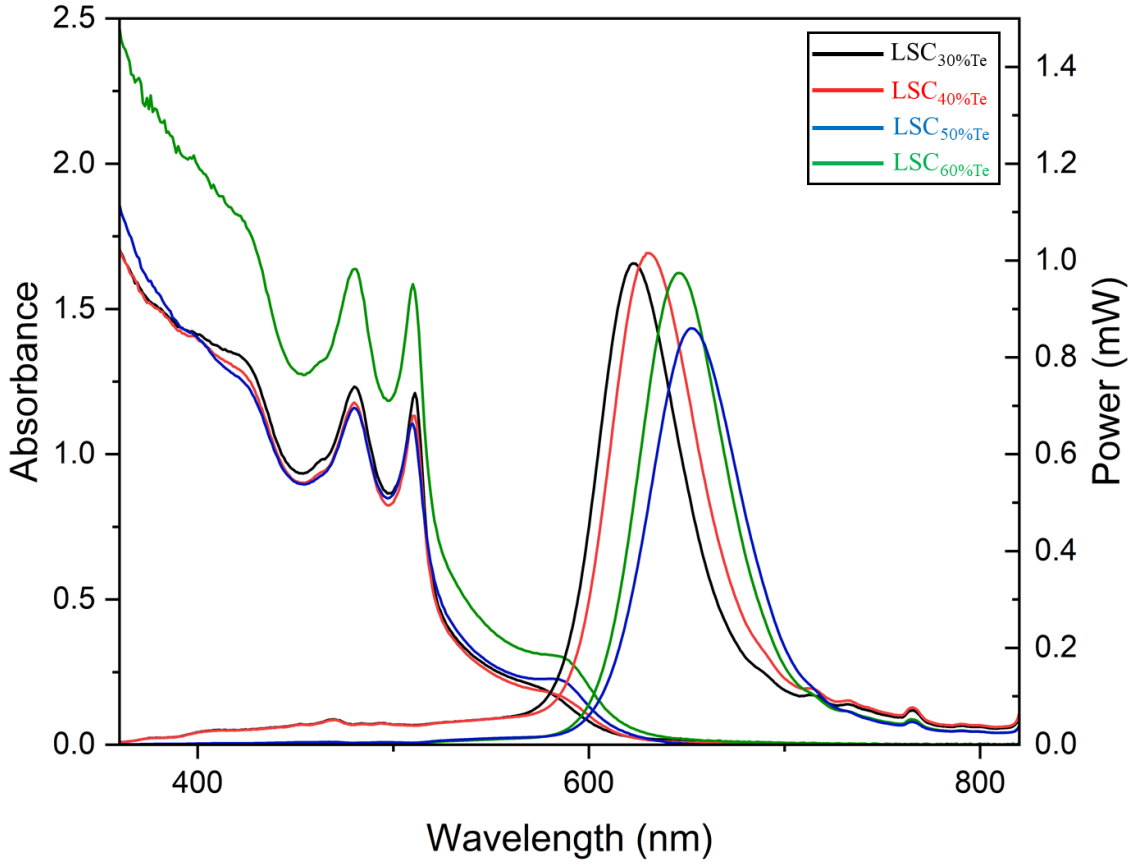

Figure 4.9. Absorbance and collected power spectra of the highest-performing LSCs parameterized with respect to the varying Te concentration used in the luminophores of the fabricated LSC devices.

Equation 4.1. represents the optical power conversion efficiency, η_{power}, where P_{out} is the total power collected from the edges of LSC and P_{in} is total power delivered to the LSC.

$$\eta_{power} = \frac{P_{out}}{P_{in}} \tag{4.1}$$

Table 4.1. Optical power conversion efficiencies and quantum yields of $CdSe/CdSe_{1-x}Te_x/CdSe/CdS$ NPLs with different compositions of tellurium (x) embedded in LSC_x.

Tellurium concentration in the luminophore of the LSC	Quantum yield of luminophore	Optical power conversion efficiency (η_{power})
$LSC_{30\%Te}$	~95%	6.91%
$LSC_{40\%Te}$	~100%	7.29%
$LSC_{50\%Te}$	~90%	5.89%
$LSC_{60\%Te}$	~89.5%	5.45%

4.5. Comparison of Results with Literature

The efficiency and performance of LSCs largely depend on the type of luminophores embedded within them, which are responsible for absorbing and re-emitting light. Among the various nanomaterials used as luminophores, type-II NPLs have garnered significant attention due to their unique optical properties including longer exciton lifetimes, reduced nonradiative recombination, high photoluminescence efficiency, and significant Stokes shift minimizing reabsorption losses. However, studies including NPLs are limited in the literature. Therefore, Table 4.2 compares the previously reported works with this thesis.

Although perovskite NCs are highly efficient as luminophores, they are infamous for their instability under environmental conditions such as moisture, heat, and light exposure. This inherent instability can considerably reduce the lifespan and reliability of perovskite-based LSCs unless extensive encapsulation and stabilization strategies are implemented. As shown in Table 4.2, the highest optical power conversion efficiency of our fabricated LSC surpasses that of the recently reported $CH_3NH_3PbBr_3$ perovskite luminophore, which has a η_{power} of 6.0%.

In addition, quantum dots' performance is often hindered by reabsorption losses and stability issues. The smaller Stokes shift in QDs leads to significant light trapping within a LSC, reducing the effective concentration of light on the PV cells. Nevertheless, $CuInS_2/ZnS$ QDs possessing relatively broad absorption range have the maximum optical power conversion efficiency (8.1%)

compared to other types of luminophores, and our best optical power conversion efficiency is not far from it.

Dyes exhibit strong absorption and emission properties across a broad range of wavelengths, and as demonstrated in Table 4.2, our highest-performing LSC shows comparable power conversion efficiency with the best-performing dye-based LSC. Previous studies indicate that increasing the concentration of luminophores in LSCs, up to a certain threshold, enhances optical power conversion efficiency by improving absorption capacity [58]. Our results are promising for further advancement by optimizing luminophore concentration. However, the chemical composition of dyes requires refinement to address challenges such as low quantum yield, photobleaching, and reabsorption losses, which compromise the long-term efficiency and stability of LSCs.

Moreover, there is no consensus in formulating the depicting figures-of-merit for the evaluation of performance of fabricated LSCs. Some consider power conversion efficiency (PCE) as an appropriate efficiency parameter, as given in Equation 4.2,

$$\mathrm{PCE} = \frac{P_{PV}}{P_{in}} \tag{4.2}$$

where P_{PV} is the electrical power generated (W), and P_{in} is the incident optical power (W). However, since this measurement approach calculates PCE together with the photovoltaics' efficiency, it is not clearly reflecting the LSC's own efficiency. Here the optical power conversion efficiency (η_{power}) or commonly optical efficiency (η_{opt}) is adopted, which could be a more meaningful parameter for the evaluation of a LSC alone.

Table 4.2. Optical efficiencies of LSCs reported for various emitter materials.

Material	**Absorption range (nm)**	**LSC dimensions (cm^3)**	(η_{opt}) %	**Ref.**
CdSe/CdSeTe/CdSe/CdS NPLs	300-650	5 x 5 x 0.1	7.29	This work
Cu: CdSe NPLs	300-470	10 × 10 × 0.1	1.65	[38]
CdSe/CdS QDs	300-650	21.5 x 1.3 x 0.5	0.6	[59]
CdSe/CdPbS QDs	300-650	7 x 1.5 x 0.3	1.4	[60]
CuInSeS/ZnS QDs	300-1000	12 x 12 x 0.3	3.27	[61]
$CuInS_2$/ZnS QDs	300-826	10 x 10 x 0.14	8.1	[62]
Si QDs	300-800	12 x 12 x 0.26	2.85	[63]
Carbazole dicyanobenzene dye	300-550	12.5 x 3 x 0.3	2.2	[64]

Benzo[1,2-d:4,5-d']bisthiazole dye	300-525	5 x 5 x 0.3	6.42	[65]
Coumarin 6 dye	300-580	5 x 5 x 0.3	7.4	[66]
$CsPb(I_xBr_{1-x})_3$ perovskite	300-625	9 x 1.3 x 0.2	2.0	[67]
$CH_3NH_3PbBr_3$ perovskite	430-620	5 x 3 x 0.5	6.0	[68]

Considering the optical power conversion efficiency values reported in the literature, using the synthesized CdSe/CdSeTe/CdSe/CdS core/multicrown type-II NPLs embedded in LSCs has enabled us to achieve results among the highest in the field.

Chapter 5

Conclusion

Increasing worldwide energy demand and global warming have intensified interest in renewable and sustainable energy research. Due to the fact that solar energy offers abundant and clean energy, the methods for harnessing solar power have drawn significant attention. LSCs offer us the ability to collect and concentrate sunlight for the mounted photovoltaic cells. Nanoplatelets are attractive as the luminophores for LSCs. Within the scope of this thesis, CdSe/CdSeTe/CdSe/CdS core/multicrown type-II NPLs with changing Te composition were synthesized as luminescent species. We employed different material characterization methods including UV-Vis absorption and PL spectroscopies. In addition, structural properties were investigated by TEM and XRD. Characterization results showed that Stokes shift can be tuned by changing Te concentration, and near-unity PL-QY can be achieved, which are crucial fabricating high-performance LSCs. We further optically characterized the resulting LSC using TRF and reabsorption measurements. The longer exciton lifetime characteristic of type-II NPL was supported by our NPL's longest lifetime of 286.4 ns.

We demonstrated several LSCs fabricated via embedding CdSe/$CdSe_{1-x}Te_x$/CdSe/CdS ($0.3 \leq x \leq 0.6$) core/multicrown NPLs with varied compositions. CdSe/$CdSe_{0.6}Te_{0.4}$/CdSe/CdS core/multicrown NPLs incorporated in the LSC exhibit the highest optical power conversion efficiency of 7.29% possessing large Stokes shift and near unity PLQY.

Our optical power conversion efficiencies indicate significant potential for large-scale LSC fabrication. By advancing the fabrication and optical characterization of these LSCs, their commercial viability can be further realized. Additionally, as previously mentioned, studies have demonstrated that the concentration of luminophores within the nanocomposite layer significantly influences the power conversion efficiency of LSCs. By increasing the concentration of nanoplatelets employed as luminophores within the polymer host matrix, it is feasible to develop new devices and achieve further performance enhancements. Moreover, alloying CdSe/CdSeTe/CdSe/CdS core/multicrown NPLs with mercury can offer the advantage of extending the absorption spectral range, thereby contributing to enhanced device efficiency.

Our highest-performing optical power conversion efficiency level is among the best of Cd-containing material systems in particular and NPLs in general, which puts the LSC of this material system on par with LSCs of the previously reported dyes (7.4%) and perovskites (6.0%) best in their classes. The best optical power conversion efficiency achieved using these type-II NPLs mark slightly below that of the $CuInS_2$/ZnS QDs LSC (8.1%) previously reported as the highest in literature. Optimization of the NPL concentration in our LSCs is necessary further to push the conversion efficiency.

Due to their affordability and scalability these type-II NPLs hold great promise in several applications of LSCs, including those for agriculture in greenhouses, construction of the facades of buildings, and aerospace together with solar panels on satellites and spacecrafts. The findings of this thesis shed light on type-II NPLs, particularly for their use in LSCs, which has not yet been fully exploited to date.

Chapter 6

Bibliography

[1] J. L. Aleixandre-Tudó, L. Castelló-Cogollos, J. L. Aleixandre, R. Aleixandre-Benavent, *Renewable Energy* **2019**, 139, 268.

[2] A. G. a. V. Wittwer, in *Advances in Solid State Physics*, Vol. 19, 1979.

[3] R. E. I. S. P. Moraitis, W.G.J.H.M. van Sark, *Optical Materials* **2018**, 84, 636.

[4] A. P. Sergei A. Ivanov, Jagjit Nanda, Sergei Tretiak, Kevin R. Zavadil, William O. Wallace, Don Werder, Victor I. Klimov and Donald J Werder, *Journal of the American Chemical Society* **2007**, 129, 11708.

[5] M. P. r. a. L. L. Peter Reiss, *Small* **2009**, 5, 154.

[6] C. d. M. Donegá, *Chemical Society Reviews* **2011**, 40, 1512.

[7] X. C. Clemens Burda, Radha Narayanan, and Mostafa A. El-Sayed, *American Chemical Society* **2005**, 105, 1025.

[8] P. D. C. Luigi Carbone, *Nano Today* **2010**, 5, 449.

[9] B. L. Yemliha Altintas, Pedro Ludwig Hernández-Martínez, Negar Gheshlaghi, Farzan Shabani, Manoj Sharma, Lin Wang, Handong Sun, Evren Mutlugun*, and Hilmi Volkan Demir, *American Chemical Society* **2020**, 32, 7874.

[10] D. J. N. C. B. Murray, and M. G. Bawendi, *Journal of the American Chemical Society* **1993**, 115, 8706.

[11] J.-S. L. Dmitri V. Talapin, Maksym V. Kovalenko, and Elena V. Shevchenko, *Chemical Reviews* **2010**, 110, 389.

[12] J. Z. Z. Damon A. Wheeler, **2013**, 25, 2878.

[13] B. K. Ridley, *Quantum processes in semiconductors*, **2013**.

[14] A. S. R. C. Joel van Embden, and Jacek J. Jasieniak, **2015**, 27, 2246.

[15] H. D. B. Farzan Shabani, Iklim Yurdakul, Savas Delikanli, Negar Gheshlaghi, Furkan Isik, Baiquan Liu, Yemliha Altintas, Betül Canımkurbey, Hilmi Volkan Demir, *Small* **2022**, 18, 2106115.

[16] M. J. E. a. B. M. Cossairt, *Chemical Communications* **2018**, 54, 7109.

[17] S. S. L. Chi-Hung Chuang, Gregory D. Scholes, and Clemens Burda, *The Journal of Physical Chemistry Letters* **2010**, 1, 2530.

[18] V. S. Marion Dufour, Eva Izquierdo, Thomas Pons, Nicolas Lequeux, Emmanuel Lhuillier, Laurent Legrand, Maria Chamarro, Thierry Barisien, and Sandrine Ithurria, *The Journal of Physical Chemistry C* **2017**, 121, 24816.

[19] B. G. Savas Delikanli, Pedro L. Hernández-Martínez, Talha Erdem, Yusuf Kelestemur, Murat Olutas, Mehmet Zafer Akgul, Hilmi V. Demir, *Advanced Functional Materials* **2015**, 25, 4282.

[20] P. S. Mickaël D. Tessier, Dorian Dupont, Gilles Patriarche, Sandrine Ithurria, and Benoit Dubertret, **2014**, 14, 207.

[21] M. O. Yusuf Kelestemur, Savas Delikanli, Burak Guzelturk, Mehmet Zafer Akgul, Hilmi Volkan Demir, *The Journal of Physical Chemistry C* **2015**, 119, 2177.

[22] S. Pedetti, S. Ithurria, H. Heuclin, G. Patriarche, B. Dubertret, *Journal of American Chemical Society* **2014**, 136, 16430.

[23] A. V. Antanovich, A. V. Prudnikau, D. Melnikau, Y. P. Rakovich, A. Chuvilin, U. Woggon, A. W. Achtstein, M. V. Artemyev, *Nanoscale* **2015**, 7, 8084.

[24] Q. Li, Z. Xu, J. R. McBride, T. Lian, *ACS Nano* **2017**, 11, 2545.

[25] N. T. Didem Dede, Ulviyya Quliyeva, Mustafa Sak, Yusuf Kelestemur, Kivanc Gungor, and Hilmi Volkan Demir, *Chemistry of Materials* **2019**, 31, 1818.

[26] B. C. Savas Delikanli, Pedro Ludwig Hernández-Martínez, Farzan Shabani, Ahmet Tarik Isik, Ilayda Ozkan, Iklim Bozkaya, Taylan Bozkaya, Furkan Isik, Emek Goksu Durmusoglu, Merve Izmir, Hakan Akgun, and Hilmi Volkan Demir, *Journal of the American Chemical Society* **2023**, 145, 12033.

[27] V. G. Corentin Dabard, Charlie Gréboval, Hong Po, Lina Makke, Ningyuan Fu, Xiang Zhen Xu, Mathieu G. Silly, Gilles Patriarche, Emmanuel Lhuillier, Thierry Barisien, Juan I. Climente, Benjamin T. Diroll & Sandrine Ithurria, *Nature Communications* **2022**, 13, 5094.

[28] B. G. Yusuf Kelestemur, Onur Erdem, Murat Olutas, Talha Erdem, Can Firat Usanmaz, Kivanc Gungor, and Hilmi Volkan Demir, *The Journal of Physical Chemistry C* **2017**, 121, 4650.

[29] S. D. Baiquan Liu, Yuan Gao, Didem Dede, Kivanc Gungor, Hilmi Volkan Demir, *Nano Energy*, 47, 115.

[30] M. L. Yuan Gao, Savas Delikanli, Haiyang Zheng, Baiquan Liu, Cuong Dang, Tze Chien Sum and Hilmi Volkan Demir, *Nanoscale* **2018**, 10, 9466.

[31] A. M. Avisek Dutta, and Amitava Patra, *The Journal of Physical Chemistry C* **2021**, 125, 20.

[32] B. T. Diroll, B. Guzelturk, H. Po, C. Dabard, N. Fu, L. Makke, E. Lhuillier, S. Ithurria, *Chemical Reviews* **2023**, 123, 3543.

[33] T. Warner, K. P. Ghiggino, G. Rosengarten, *Solar Energy* **2022**, 246, 119.

[34] L. R. Bradshaw, K. E. Knowles, S. McDowall, D. R. Gamelin, *Nano Letters* **2015**, 15, 1315.

[35] Z. Krumer, S. Pera, R. Moes, Y. Zhao, A. Brouwer, E. Groeneveld, W. van Sark, R. E. I. Schropp, C. Donega, *Solar Energy Materials and Solar Cells* **2012**, 111, 57.

[36] I. Coropceanu, M. G. Bawendi, *Nano Letters* **2014**, 14, 4097.

[37] C. S. Erickson, L. R. Bradshaw, S. McDowall, J. D. Gilbertson, D. R. Gamelin, D. L. Patrick, *ACS Nano* **2014**, 8, 3461.

[38] M. Sharma, K. Güngör, A. Yeltik, M. Olutas, B. Guzelturk, Y. Kelestemur, T. Erdem, S. Delikanli, J. McBride, H. Demir, *Advanced Materials* **2017**, 1700821.

[39] J. Liu, Q. Zhao, J.-L. Liu, Y.-S. Wu, Y. Cheng, M.-W. Ji, H.-M. Qian, W.-C. Hao, L.-J. Zhang, X.-J. Wei, S.-G. Wang, J.-T. Zhang, Y. Du, S.-X. Dou, H.-S. Zhu, *Advanced Materials* **2015**, 27, 2753.

[40] K. E. Knowles, K. H. Hartstein, T. B. Kilburn, A. Marchioro, H. D. Nelson, P. J. Whitham, D. R. Gamelin, *Chem Rev* **2016**, 116, 10820.

[41] M. Olutas, B. Guzelturk, Y. Kelestemur, A. Yeltik, S. Delikanli, H. V. Demir, *ACS Nano* **2015**, 9, 5041.

[42] A. Yeltik, S. Delikanli, M. Olutas, Y. Kelestemur, B. Guzelturk, H. V. Demir, *The Journal of Physical Chemistry C* **2015**, 119, 26768.

[43] C. She, I. Fedin, D. S. Dolzhnikov, P. D. Dahlberg, G. S. Engel, R. D. Schaller, D. V. Talapin, *ACS Nano* **2015**, 9, 9475.

[44] J. M. Pietryga, Y.-S. Park, J. Lim, A. F. Fidler, W. K. Bae, S. Brovelli, V. I. Klimov, *Chemical Reviews* **2016**, 116, 10513.

[45] Y. Kelestemur, M. Olutas, S. Delikanli, B. Guzelturk, M. Akgül, H. Demir, *The Journal of Physical Chemistry C* **2015**, 119, 2177.

[46] Y. Kelestemur, B. Guzelturk, O. Erdem, M. Olutas, T. Erdem, C. F. Usanmaz, K. Gungor, H. V. Demir, *The Journal of Physical Chemistry C* **2017**, 121, 4650.

[47] D. Dede, N. Taghipour, U. Quliyeva, M. Sak, Y. Kelestemur, K. Gungor, H. V. Demir, *Chemistry of Materials* **2019**, 31, 1818.

[48] Y. Altintas, B. Liu, P. L. Hernández-Martínez, N. Gheshlaghi, F. Shabani, M. Sharma, L. Wang, H. Sun, E. Mutlugun, H. V. Demir, *Chemistry of Materials* **2020**, 32, 7874.

[49] M. D. Tessier, P. Spinicelli, D. Dupont, G. Patriarche, S. Ithurria, B. Dubertret, *Nano Lett* **2014**, 14, 207.

[50] K. Rasmussen, H. Rauscher, A. Mech, in *Adverse Effects of Engineered Nanomaterials (Second Edition)*, (Eds: B. Fadeel, A. Pietroiusti, A. A. Shvedova), Academic Press, 2017.

[51] E. F. Chagas, E. S. Ferreira, in *Ferrite Nanostructured Magnetic Materials*, (Eds: J. Pal Singh, K. H. Chae, R. C. Srivastava, O. F. Caltun), Woodhead Publishing, 2023.

[52] G. F. Harrington, J. Santiso, *Journal of Electroceramics* **2021**, 47, 141.

[53] J. S. Rigden, *Macmillan Encyclopedia of Physics*, Simon & Schuster Macmillan, **1996**.

[54] S. Pedetti, S. Ithurria, H. Heuclin, G. Patriarche, B. Dubertret, *J Am Chem Soc* **2014**, 136, 16430.

[55] S. Delikanli, B. Canimkurbey, P. L. Hernández-Martínez, F. Shabani, A. T. Isik, I. Ozkan, I. Bozkaya, T. Bozkaya, F. Isik, E. G. Durmusoglu, M. Izmir, H. Akgun, H. V. Demir, *Journal of the American Chemical Society* **2023**, 145, 12033.

[56] L. Liao, T. Lin, X. Bin, K. Quan, L. Zhang, R. Zeng, J. Zhai, X. Mo, J. Zhao, *Journal of Luminescence* **2022**, 248, 118927.

[57] B. Richards, I. Howard, *Energy & Environmental Science* **2023**, 16.

[58] Z. Krumer, W. G. J. H. M. van Sark, R. E. I. Schropp, C. de Mello Donegá, *Solar Energy Materials and Solar Cells* **2017**, 167, 133.

[59] F. Meinardi, A. Colombo, K. A. Velizhanin, R. Simonutti, M. Lorenzon, L. Beverina, R. Viswanatha, V. I. Klimov, S. Brovelli, **2014**, 8.

[60] H. Zhao, D. Benetti, L. Jin, Y. Zhou, F. Rosei, A. Vomiero, *Small* **2016**, 12, 5368.

[61] F. Meinardi, H. McDaniel, F. Carulli, A. Colombo, K. A. Velizhanin, N. S. Makarov, R. Simonutti, V. I. Klimov, S. Brovelli, *Nat Nanotechnol* **2015**, 10, 878.

[62] M. R. Bergren, N. S. Makarov, K. Ramasamy, A. Jackson, R. Guglielmetti, H. McDaniel, *ACS Energy Letters* **2018**, 3, 520.

[63] F. Meinardi, S. Ehrenberg, L. Dhamo, F. Carulli, M. Mauri, F. Bruni, R. Simonutti, U. Kortshagen, S. Brovelli, *Nature Photonics* **2017**, 11, 177.

[64] F. Mateen, S. Y. Lee, S.-K. Hong, *Journal of Materials Chemistry A* **2020**, 8, 3708.

[65] C. Papucci, T. A. Geervliet, D. Franchi, O. Bettucci, A. Mordini, G. Reginato, F. Picchioni, A. Pucci, M. Calamante, L. Zani, *European Journal of Organic Chemistry* **2018**, 2018, 2657.

[66] M. Sottile, G. Tomei, S. Borsacchi, F. Martini, M. Geppi, G. Ruggeri, A. Pucci, *European Polymer Journal* **2017**, 89, 23.

[67] H. Zhao, Y. Zhou, D. Benetti, D. Ma, F. Rosei, *Nano Energy* **2017**, 37, 214.

[68] E. Bagherzadeh-Khajehmarjan, A. Nikniazi, B. Olyaeefar, S. Ahmadi-Kandjani, J.-M. Nunzi, *Solar Energy Materials and Solar Cells* **2019**, 192, 44.